Doctoral Dissertation (Censored)
博士論文（要約）

Studies on the comprehensive generation of various
phyllotactic patterns with a predominant focus on uncommon
phyllotaxes

（特異な葉序に着目した多様な葉序パターンの包括的生成に
関する研究）

Takaaki Yonekura
米倉　崇晃

Acknowledgements

Abstract

Plant leaves are arranged around the stem in a beautiful geometry that is called phyllotaxis. In the majority of plants, phyllotactic patterns are restricted to a few types, such as distichous, Fibonacci spiral, decussate, and tricussate, which share some mathematical features. To explain the regularity and limited variety of phyllotactic patterns, many researchers have studied with various approaches.

Phyllotactic patterning reflects the positional relationship of a new leaf primordium to the existing leaf primordia at the shoot apex. Already in the early days, repulsive interaction between leaf primordia was hypothesized from morphological analysis to be a key of spatial regulation of new leaf primordium formation and phyllotactic pattering. Based on this notion, many theoretical models have been proposed. Among them, particularly notable are the two mathematical models proposed by Douady and Couder (alternate-specific form, DC1; more generalized form, DC2), the central assumptions of which are that each leaf primordium emits a constant power that inhibits new primordium formation and that this inhibitory effect decreases with distance. It was demonstrated by computer simulations that any major type of phyllotaxis can occur as a self-organizing stable pattern in the framework of DC models.

However, several phyllotactic types remain unaddressed. One interesting example is orixate phyllotaxis, which has a tetrastichous alternate pattern with four-cycle periodic repetition of a sequence of different divergence angles: 180°, 90°, 180°, and 270°. Although the term orixate phyllotaxis was derived from *Orixa japonica*, this type is observed in several distant taxa, suggesting that it may represent some aspects of a common mechanism of phyllotactic patterning. If DC models cannot produce orixate phyllotaxis, it should indicate that they are incomplete for the general framework of generation of phyllotactic patterns. The incompleteness of DC models is also suggested from the disagreement between the natural occurrence and DC model simulations in how dominant the Fibonacci spiral is in spiral patterns: the Fibonacci spiral is highly dominant in nature while it is only moderately dominant in the DC model simulations.

Moreover, there are a few types of phyllotaxis that challenge the basic concept of DC and many other models. The most conspicuous one is costoid phyllotaxis. Costoid phyllotaxis is unique to Costaceae, and is characterized by a steep spiral with a small divergence angle, which indicates that a new primordium arises near its preceding primordium. Because this character seems to conflict with the repulsive interaction between leaf primordia widely accepted as the ground of phyllotactic patterning in the previous studies, costoid phyllotaxis is called a "genuine puzzle".

In the studies described in this thesis, to explore the fundamental mechanism of leaf primordium positioning that can produce all variety of naturally found phyllotactic patterns in reasonable proportions, I performed morphological and mathematical model analyses with a predominant focus on the two unsolved types of phyllotaxis, orixate phyllotaxis and costoid phyllotaxis.

At first, I investigated the morphological features of real orixate phyllotaxis and the theoretical requirements for the generation of orixate phyllotaxis. Close observation of the winter buds of *O. japonica* confirmed that the phyllotaxis of this plant is truly orixate and showed that the plastochron ratio oscillates in relation to the divergence angle. For mathematical modeling, I examined DC models regarding the ability to

produce orixate phyllotaxis and found that model expansion via the introduction of primordial age-dependent changes of the inhibitory power is absolutely necessary for the establishment of orixate phyllotaxis. The orixate patterns generated by the expanded version of DC2 (EDC2) were shown to share morphological details with real orixate phyllotaxis. Furthermore, the simulation results obtained using EDC2 fitted better the natural distribution of phyllotactic patterns for the dominance of Fibonacci spiral in spiral phyllotaxis than did those obtained using the previous models. These findings indicate that EDC2 is suitable for sufficiently representing the general framework of phyllotactic patterning.

At the molecular level, the initial stage of leaf primordium development is believed to be controlled by the plant hormone auxin in such a way that a positive feedback loop between auxin gradient and auxin polar transport spontaneously creates auxin convergence to trigger primordium initiation, which was previously integrated into mathematical models. By comparison with these auxin-transport-based models, I next considered the possibility that the age-dependent increase of the inhibitory power in EDC models may reflect expansion of the area surrounding an auxin convergence point toward which auxin is drained by polar transport. Meaningful expansion of the auxin drainage area was found by theoretical analysis not to occur under the constant dynamics of the auxin polar transport. Then I modified the auxin-transport-based model by superimposing changes in the auxin transport property within each primordium on the basic auxin transport dynamics to force the auxin drainage area to expand with the age of the primordium. In computer simulations with this modified auxin model, orixate-phyllotaxis-like patterns were generated at several conditions causing late and slow expansion of the auxin drainage area. These patterns, however, were always unstable, which implicated some additional mechanisms for the stabilization of orixate phyllotaxis.

Finally, I examined the requirements for the generation of costoid phyllotaxis taking EDC2 as a starting point. By morphological analysis of costoid phyllotaxis of *Costus megalobractea*, I found that it shows not only a small divergence angle but also a large plastochron ratio. These characters implied that some kind of attractive interaction between leaf primordia acts as a control factor in the positioning of a new leaf primordium. Thus, I added a hypothetical effect of the preceding primordium that induces primordium formation in its vicinity into EDC2 to construct a new model consisting of both inductive and inhibitory fields (named YS model for the Japanese words "Yūdou" for induction and "Sogai" for inhibition). Whereas computer simulations with YS model returned the same results as did those with EDC2 at a wide range of conditions and failed to form leaf primordia at another wide range of conditions, simulations within the narrow range between these two conditions, where increases in the inductive and inhibitory effects were competed in a balanced relation, produced costoid phyllotaxis as a stable pattern. In computer simulations within this range, one-sided distichous phyllotaxis was generated as well in dependence on slight changes in the parameter settings. As both one-sided distichous and costoid phyllotaxes occur characteristically in Zingiberales, the results of the computer simulations seem to reasonably reflect phyllotactic patterning in this plant group. In observation of growing seedlings of *C. megalobractea*, I noticed that the divergence angle is relatively large between early leaves and is smaller between later leaves. Assuming a gradual increase of the SAM size during seedling growth, which is common among plants, such change in the divergence angle was reproduced by computer simulation with YS model. This result also supports the validity of YS model.

In summary, the present studies revealed that the primordial age-dependent increase of the inhibitory power of the existing leaf primordia negatively acting on new primordium initiation is generally an important component of the mechanism of spatial regulation of leaf primordium formation and phyllotactic patterning and that its slowness and lateness are particularly essential to the generation of orixate phyllotaxis. They also suggested involvement of some inductive effect from the preceding primordium in leaf positioning for the first time and showed that the competitive expansion of the inductive and inhibitory fields can account for the generation of costoid phyllotaxis. Inquiry into the molecular basis of these interactions would cultivate a better understanding of the fundamental mechanism of phyllotactic pattern generation.

Table of Contents

List of abbreviations and parameters

Abbreviations

DC	Douady and Couder
EDC	Expanded DC
FAA	Formalin-Acetic acid-Alcohol
PIN	PIN-FORMED
SAM	Shoot Apical Meristem
SEM	Scanning Electron Microscope
YS	Yūdou and Sogai
YUC	YUCCA

Chapter II

A	rate of the age-dependent changes in the inhibitory power in EDC2
a	rate of the age-dependent changes in the inhibitory power in EDC1
B	timing of the age-dependent changes in the inhibitory power in EDC2
b	timing of the age-dependent changes in the inhibitory power in EDC1
d	distance
d_0	maximum distance within which an existing primordium excludes new primordia (inhibition range)
E	function of the inhibitory effect from single primordium dependent on the distance
E_s	given threshold of the inhibitory field strength in DC2 and EDC2
F	function of the inhibitory effect from single primordium dependent on the primordial age
G	standardized plastochron time (natural log of the plastochron ratio)
I	inhibitory field strength
k	proportional coefficient of the inhibitory power
L	primordium (numbered from the oldest one)
M	SAM periphery represented by circle
N	sine of the half of the apical angle of a cone representing shoot apex
n	primordium number
O	center of the shoot apex
P	primordium (numbered from the visible youngest one)
p	divergence angle
q	divergence angle
r	radial distance from the center of shoot apex
R_0	radius of the circle M
T	plastochron time
t	standardized primordial age
V	velocity of primordia moving away from the center of shoot apex

α	inversely proportional coefficient of the inhibitory power in DC2 and EDC2
Γ	maximum distance within which an existing primordium excludes new primordia standardized to the size and shape of shoot apex
Δt_{sim}	simulation time step
η	inversely proportional coefficient of the inhibitory power in DC1 and EDC1
θ	radial angle
θ^*	divergence angle
$\varrho(r)$	$\sqrt{r^2 + 1}$
ψ	apical angle of the cone representing shoot apex

Chapter III

A	rate of the age-dependent changes in the inhibitory power in EDC2
A_i	auxin amount in cell i
a_i	apparent auxin concentration in cell i
$A_{\Re}$	rate of the age-dependent expansion of the range of auxin drainage area
a_{Th}	auxin concentration threshold of primordium initiation
B	timing of the age-dependent changes in the inhibitory power in EDC2
$B_{\Re}$	timing of the age-dependent expansion of the range of auxin drainage area
C	curved surface representing shoot apex
c	auxin production rate
c_{cyc}	cell cycle
c_{cen}	auxin production rate in central zone
$\boldsymbol{C_i}$	center of cell i
c_{per}	auxin production rate in SAM periphery
c_{pri}	auxin production rate in primordia
c_{pro}	auxin production rate in proximal zone
D	diffusion coefficient
d	auxin degradation rate
d_{ex}	inhibition range
d_0	maximum distance within which an existing primordium excludes new primordia in EDC2
E	function of the inhibitory effect from single primordium dependent on the distance in EDC2
E_s	given threshold of the inhibitory field strength in EDC2
F	function of the inhibitory effect from single primordium dependent on the primordial age in EDC2
f	function of the curved surface representing shoot apex
$F_n(\boldsymbol{r})$	magnitude of force to restrict vertex on given curved surface at the position $\boldsymbol{r}$
G	standardized plastochron time (natural log of the plastochron ratio)
g_d	geodesic distance
G_{large}	large one of the oscillating natural log of plastochron ratio

G_{small}	small one of the oscillating natural log of plastochron ratio
$\mathcal{R}$	radius of auxin drainage area
$\mathcal{R}_{max}$	maximum radius of auxin drainage area
J	auxin flux
k	quadratic coefficient of the paraboloid of revolution
K_b	strength of line tension
K_s	strength of the elastic coefficient
k_{time}	time that single primordium takes to leave e times away from the center of shoot apex
$\boldsymbol{K}_{uv}$	coefficient matrix of the equation of motion
k_1	PIN membrane localization rate
k_2	PIN internalization rate
l_{ij}	cell wall length between cell i and cell j
l_{cell}	cell length
n	number of primordia
n^*	modified number of primordia
$\boldsymbol{n}_f(\boldsymbol{r})$	surface normal vector at the position $\boldsymbol{r}$
$\mathcal{N}(i)$	set of cells neighboring cell i
P	total PIN amount
P_i	PIN amount in cytosol of cell i
$P_{i \rightarrow j}$	PIN amount on the membrane of cell i faced to cell j
$\boldsymbol{P}_m$	center of primordium m
$\boldsymbol{r}$	position of cell vertex displayed in rectangular coordinate
r_{cen}	radius of central zone
r_{per}	radius of SAM periphery
r_{pro}	radius of proximal zone
$\boldsymbol{r}_{r\theta}$	position of cell vertex displayed in polar coordinate
S_i	area of cell i
s_0	suitable cell area
T	PIN activity
Ti	passing time from winter bud produced
t_s	passing time in a single step in the simulation
t_{sim}	passing time in the simulation
v_c	auxin transport rate to the neighboring cell
v_l	mean velocity of auxin
α	inversely proportional coefficient of the inhibitory power in DC2 and EDC2
$\delta \boldsymbol{r}$	step size for solving partial derivative
Δt_{sim}	simulation time step
η	viscous coefficient of cell vertex

κ	PIN saturation coefficient
μ	cell polarity of auxin transport
μ_c	mean value of cell cycle
σ_c	standard deviation of cell cycle

Chapter IV

A	rate of the age-dependent changes in the inhibitory power in EDC2
a	rate of the age-dependent changes in the inhibitory power in EDC1
A_S	rate of the age-dependent changes in the inhibitory power
A_Y	rate of the age-dependent changes in the inductive power
B	timing of the age-dependent changes in the inhibitory power in EDC2
b	timing of the age-dependent changes in the inhibitory power in EDC1
B_S	timing of the age-dependent changes in the inhibitory power
B_Y	timing of the age-dependent changes in the inductive power
d	distance
d_S	maximum inhibition range
d_Y	maximum induction range
E_S	function of the inhibitory effect from single primordium dependent on the distance
E_Y	function of the inductive effect from single primordium dependent on the distance
F_S	function of the inhibitory effect from single primordium dependent on the primordial age
F_Y	function of the inductive effect from single primordium dependent on the primordial age
G	standardized plastochron time (natural log of the plastochron ratio)
G_S	G value calculated from the YS model simulation without considering the inductive effect
L	primordium (numbered from the oldest one)
M	SAM periphery represented by circle
N	sine of the half of the apical angle of a cone representing shoot apex
n	primordium number
O	center of the shoot apex
P	primordium (numbered from the visible youngest one)
p	divergence angle
q	divergence angle
r	radial distance from the center of shoot apex
R_0	radius of the circle M
R_{0f}	limiting value of the radius of the circle M at $t \to \infty$
S	inhibitory field strength
S_{th}	inhibitory field strength threshold for primordium initiation
T	plastochron time
t	standardized primordial age

t_i timing of the SAM enlargement

t_{sim} passing time in the simulation

U internal energy of shoot apex

V velocity of primordia moving away from the center of shoot apex

w distance normalized by the size and the shape of shoot apex

w^* distance normalized by the shape of shoot apex

Y inductive field strength

Y_{th} inductive field strength threshold for primordium initiation

α inversely proportional coefficient of the inhibitory power in EDC2

α_S inversely proportional coefficient of the inhibitory power

α_Y inversely proportional coefficient of the inductive power

Γ maximum inhibition range standardized to the size and the shape of shoot apex in EDC2

Γ_S maximum inhibition range standardized to the size and the shape of shoot apex

Γ_{S_f} limiting value of the maximum inhibition range standardized to the size and the shape of shoot apex at $t \rightarrow \infty$

Γ_{S_i} limiting value of the maximum inhibition range standardized to the size and the shape of shoot apex at $t \rightarrow -\infty$

Γ_Y maximum induction range standardized to the size and the shape of shoot apex

Γ_{Y_f} limiting value of the maximum induction range standardized to the size and the shape of shoot apex at $t \rightarrow \infty$

Δt plastochron times in the simulation

Δt_{sim} simulation time step

η inversely proportional coefficient of the inhibitory power in EDC1

θ radial angle

τ gentleness of the SAM enlargement

ψ apical angle of the cone representing shoot apex

Chapter I

Preface

Living things display various well-ordered patterns both at the cell and organ levels. These patterns generally arise from less-ordered states via spontaneous and repetitive morphogenetic processes. While animals form almost all organs during embryogenesis, plants continue to form organs throughout the life span, which creates more ordered patterns postembryonically in their bodies (Weigel and Jürgens, 2002). In this respect, postembryonic development of plant organs is an important subject of study of biological patterning.

One of the most conspicuous patterns of plant organs can be seen in the regular arrangement of leaves around the stem, which is termed phyllotaxis. Across diverse plant species, phyllotaxis has common characteristics, which are often described mathematically and are reflected in a limited variety of phyllotactic patterns, including the distichous (the leaves alternating in plane), decussate (two leaves arise at one node and the pairs of leaves rotating successively by 90°), tricussate (three leaves arise at one node), and Fibonacci spiral (spiral with a divergence angle close to the golden angle of 137.5°) patterns (Figure 1-1A – D) (Green, 1992).

The origin of the regularity of, and the few particular patterns that are allowed in, phyllotaxis have long been fascinating questions for botanists. In the early days, morphological studies attributed phyllotactic patterning to Hofmeister's axiom, which claims that, on the periphery of the shoot apical meristem (SAM), a new leaf primordium is formed in the largest gap between existing primordia and as far away as possible from them (Hofmeister, 1868). Following this axiom, many theoretical models have been proposed to explain the generation of phyllotactic patterns: contact pressure models (Snow and Snow, 1962; Adler, 1974; Mitchson, 1977; Roberts, 1977; Hotton et al., 2006), repulsive energy models (Levitov, 1991a; 1991b; 1991c; Douady and Couder, 1992; 1996a; 1996b; 1996c), mechanics-based models (Green, 1992; Green et al., 1996; Shipman and Newell, 2004), and reaction-diffusion models (Turing, 1952; Meinhardt, 1982; Bernasconi, 1994). Such theoretical models are based on a common concept: the existence of an inhibitory field created by a repulsive, either physical or chemical, interaction between leaf primordia, which conforms to Hofmeister's axiom. Among them, the two mathematical models proposed by Douady and Couder (Douady and Couder, 1992; 1996a; 1996b; 1996c) are particularly notable (they will be referred to as DC1 and DC2 hereafter). The key assumptions shared by DC models are that each individual leaf primordium emits a constant power that inhibits the production of a new primordium in its vicinity and that the inhibitory effect of this power decreases as the distance from the emission point increases. In DC1, a new primordium arises one by one at a constant time interval, i.e., plastochron, at a point on the periphery of the shoot apical meristem (SAM) where the inhibitory field strength is smallest. In DC2, when the inhibitory field strength falls below a given threshold somewhere on the SAM periphery, a new primordium is formed immediately at that point. Computer simulations using DC models demonstrated that they can generate various common phyllotactic patterns as stable patterns that depend on parameter settings (Douady and Couder, 1992; 1996a; 1996b).

In the early 2000s, experimental studies showed that auxin determines the initiation of shoot lateral organs, such as leaves and lateral buds, and that its polar transport serves as a driving force of phyllotactic patterning (Reinhardt et al., 2000; 2003; Benková et al., 2003). Briefly, the auxin efflux carrier PIN1, which is localized asymmetrically in epidermal cells of the shoot apex, polarly transports auxin to create auxin convergence, thus directing the position of lateral organ initiation. Subsequently, assuming the existence of a positive feedback

regulatory loop between the auxin concentration gradient and PIN1 localization, a novel mathematical model was developed to explain the spontaneous formation of the auxin convergence. It was further shown by computer simulation analysis that these models can produce several typical patterns of common phyllotaxis (Smith et al., 2006a; Jönsson et al., 2006). In the auxin-transport-based models, auxin polar transport toward the auxin convergence removes auxin from its surroundings, which prevents the formation of a new, vicinal auxin convergence. This effect is considered to correspond to the repulsive interaction between primordia described in the previous models. The parameters of the auxin-transport-based model were mapped on the parameters of DC2 (Newell et al., 2008; Mirabet et al., 2012), which shows that DC2 can be treated as an abstract model of the auxin-transport-based models. The auxin-transport-based models have been further examined theoretically in consideration of the relationship to the auxin canalization model (Bayer et al., 2009), of the significance of the apoplast (Fujita and Kawaguchi, 2018), and of the influence of mechanical stress (Rueda-Contreras et al., 2018).

DC models and the auxin-transport-based models, DC2 in particular, have been studied extensively regarding the ability to produce the various phyllotactic patterns that are observed in nature (Douady and Couder, 1992; 1996a; 1996b; 1996c; Smith et al., 2006a; Jönsson et al., 2006). However, several uncommon types have never been addressed in the studies that used these models. An interesting example is orixate phyllotaxis, which has a tetrastichous alternate pattern with four-cycle periodic repetition of a sequence of different divergence angles: 180°, 90°, 180°, and 270° (Maekawa, 1948). Although the term orixate phyllotaxis was derived from *Orixa japonica*, this type is observed in several distant taxa (Troll, 1937; Maekawa, 1948; Snow, 1958), suggesting that it may represent some aspects of a common mechanism of phyllotactic patterning. If DC models cannot produce orixate phyllotaxis, it should indicate that they are incomplete for the general framework of generation of phyllotactic patterns. The incompleteness of DC models is also suggested from the disagreement between the natural occurrence and DC model simulations in how dominant the Fibonacci spiral is in spiral patterns: the Fibonacci spiral is highly dominant in nature while it is only moderately dominant in the DC model simulations (Okabe, 2016).

Moreover, there are a few types of phyllotaxis that challenge the basic concept of DC and many other models. The most striking one is costoid phyllotaxis (Jean, 1994). Costoid phyllotaxis is unique to Costaceae, and is characterized by a steep spiral with a small divergence angle, which indicates that a new primordium arises near its preceding primordium. Because this character seems to conflict with Hofmeister's axiom widely accepted as the ground of phyllotactic patterning in the previous studies, costoid phyllotaxis is called a "genuine puzzle" (Jean, 1994).

In the studies described in this thesis, to explore the fundamental mechanism of leaf primordium positioning that can produce all variety of naturally found phyllotactic patterns, I performed mathematical model analyses with a predominant focus on several uncommon phyllotaxes, orixate phyllotaxis and costoid phyllotaxis. In Chapter II, after investigating the morphological features of real orixate phyllotaxis and the theoretical requirements for the generation of orixate phyllotaxis, I constructed expanded versions of DC models (EDC1 for DC1 and EDC2 for DC2) by introducing age-dependent changes into the inhibitory power. Computer simulations with EDC models revealed that the primordial age-dependent increase of the inhibitory power is generally an important

component of the mechanism of phyllotactic patterning and that slow and late increase is critical for the generation of orixate phyllotaxis. In Chapter III, I considered the possible molecular basis of the age-dependent increase of the inhibitory power in reference to the auxin-transport-based models. In Chapter IV, following morphological observations of real costoid phyllotaxis, I examined the requirements for the generation of costoid phyllotaxis taking EDC2 as a starting point. Then I added a putative effect of the preceding primordium that induces primordium formation in its vicinity into EDC2 to construct a new model consisting of both inductive and inhibitory fields (named YS model for the Japanese words "Yūdou" for induction and "Sogai" for inhibition), and finally succeeded with YS model in reproducing substantially all common and uncommon phyllotactic patterns including costoid phyllotaxis. In Chapter V, I summarized conclusions from my findings and discussed the future perspectives.
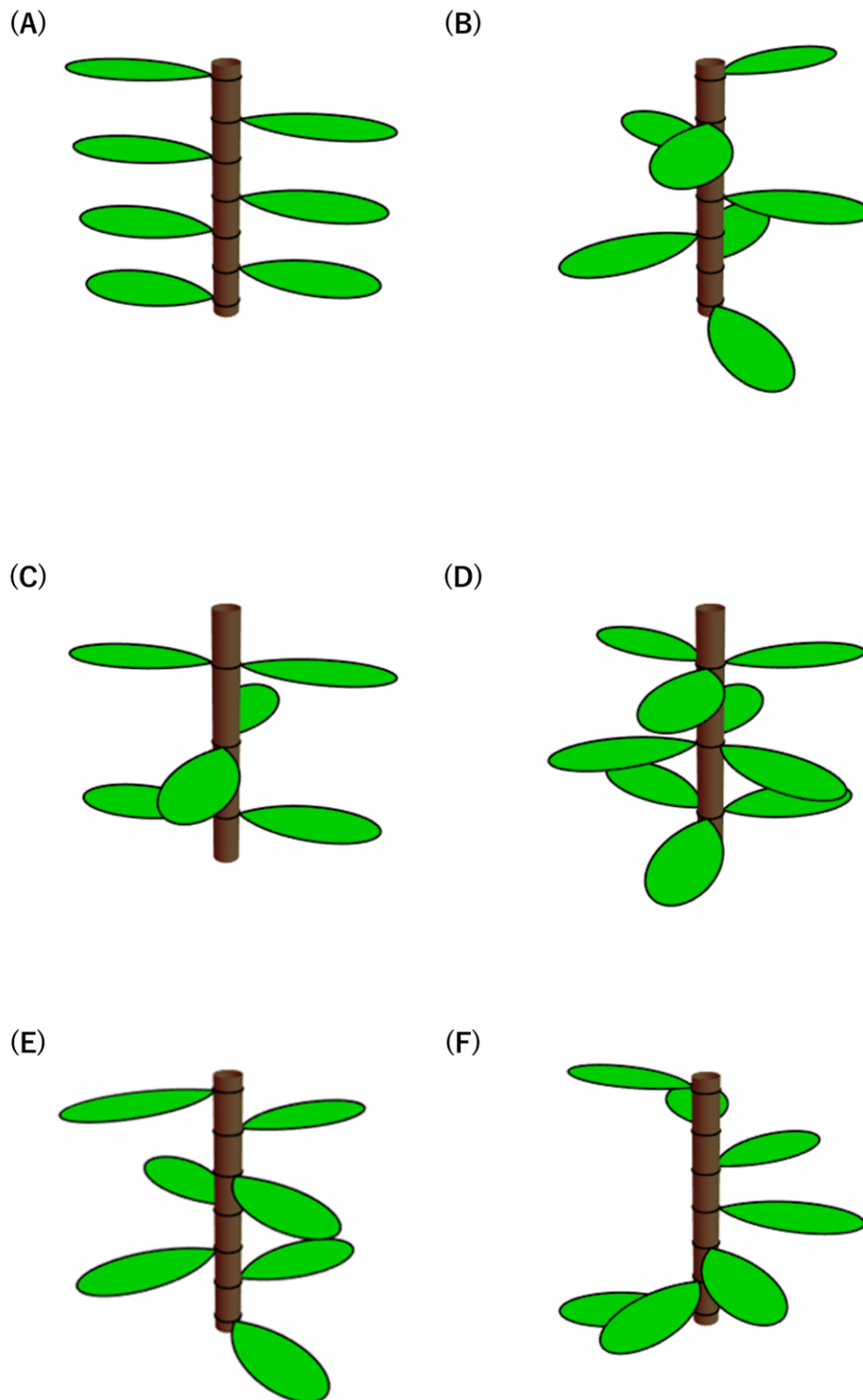
Fig 1-1. Schematic views of major and minor phyllotactic patterns in nature

(A) Distichous. (B) Spiral. (C) Decussate. (D) Tricussate. (E) Orixate phyllotaxis. (F) Costoid phyllotaxis.

16

Chapter II

Examination of the requirements for the generation of orixate phyllotaxis

Introduction

A long history of research on phyllotactic pattern formation has resulted in the establishment of two classes of models that are capable of producing many patterns of naturally occurring phyllotaxes and are now widely accepted. One class is composed of abstract models of the inhibitory-field type, represented by DC models of (Douady and Couder 1992; 1996a; 1996b; 1996c), and the other class is the auxin-transport-based models constructed by integrating molecular biological findings on the roles of auxin and its polar transport in phyllotactic patterning (Jönsson et al., 2006; Smith et al., 2006).

Of these models, DC models are most notable as the theoretical framework of leaf primordium positioning that determines phyllotactic patterns. The key assumptions shared by DC models are that each individual leaf primordium emits a constant power that inhibits the production of a new primordium near it and that the inhibitory effect of this power decreases as the distance from the emission point increases. In DC1, it is additionally assumed that leaf primordia are formed one by one at a constant time interval, i.e., plastochron; thus, DC1 deals only with alternate phyllotaxis (Douady and Couder, 1992; Douady and Couder, 1996a). In contrast, DC2 does not deny the simultaneous formation of leaf primordia or temporal changes of the plastochron and can deal with both alternate and whorled phyllotaxis (Douady and Couder, 1996b).

Computer simulations with DC models have been performed to examine how various phyllotactic patterns that are observed in nature can be generated by these models (Douady and Couder 1996b; 1996c). Although the previous results showed that the major alternate phyllotactic patterns such as distichy and Fibonacci spiral can arise as self-organizing stable patterns in DC1 and that most of the common phyllotactic patterns including decussate and tricussate patterns can arise in DC2, several types of phyllotaxis have remained unaddressed. An interesting example is orixate phyllotaxis, which is named after *Orixa japonica* (Rutaceae, Sapindales) (Maekawa, 1948). Orixate phyllotaxis is a tetrastichous alternate phyllotaxis that is characterized by the periodic repetition of a sequence of different divergence angles: 180°, 90°, −180° (180°), and −90° (270°). Although plant species that show orixate phyllotaxis are uncommon, they are found in several distant taxa (Fig 2-1). Many species of *Kniphofia* (Asphodelaceae, Asparagales) display a tetrastichous arrangement of leaves (Berger, 1908), and *K. uvaria*, *K. pumila*, and *K. tysonii* exhibit orixate phyllotaxis (Troll, 1937; Snow 1958). *Lagerstroemia indica* (Lythraceae, Myrtales) and *Berchemiella berchemiaefolia* (Rhamnaceae, Rosales) are also known as species with orixate phyllotaxis (Maekawa, 1948). The rare and sporadic distribution of orixate phyllotaxis among plants suggests that this peculiar phyllotaxis occurred independently a few times during plant evolution. Therefore, it is likely that orixate phyllotaxis is generated by a common regulatory mechanism of leaf-primordium formation under some particular condition rather than by an orixate-unique mechanism. If this is true, mathematical models that account fully for the spatial regulation of leaf-primordium formation should be able to produce not only major phyllotactic patterns, but also orixate phyllotaxis.

In this chapter, I re-examined the original DC models exhaustively under various parameter conditions, to test whether they can produce orixate phyllotaxis. I then expanded DC models by introducing primordial age-dependent changes in the inhibitory power. These results indicate that a late and slow increase in the

inhibitory power is critical for the establishment of orixate phyllotaxis and imply that changing the inhibitory power is generally an important component of the mechanism of phyllotactic patterning.

Material, methods, and models

Plant material

Terminal winter buds of *O. japonica* that had been collected in July from nine plants growing at the Koishikawa Botanical Gardens, Graduate School of Science, The University of Tokyo were used for morphological analyses.

Microscopic observation of winter buds

The winter buds were fixed with 5% v/v formalin, 5% v/v acetic acid, 50% v/v ethanol (FAA), dehydrated in an ethanol series, and finally infiltrated in 100% ethanol. For light microscopic observation, the dehydrated samples were embedded in Technovit 7100, cut into 5-μm-thick sections using a rotary microtome, and stained with 0.5% w/v toluidine blue. The center of gravity was determined for each leaf primordium on the section with ImageJ (https://imagej.nih.gov) and was used as its position when measuring morphometric data.

For scanning electron microscopy (SEM), the dehydrated samples were infiltrated once with a 1:1 v/v mixture of ethanol and isoamyl acetate and twice with isoamyl acetate. Subsequently, the samples were critical point dried, sputter coated with gold–palladium, and observed using SEM (Hitachi S-3400N).

DC1 model

The essential points of the DC1 model are as follows (Douady and Couder, 1992; 1996a).

1. The shoot apex is considered as a plane.
2. Each leaf primordium L emits a constant level of an inhibitory power, which generates an inhibitory field around it.
3. The inhibitory field strength decreases as a function of the distance, d.
4. Formation of new primordia is restricted to the SAM periphery represented by the circle M with a radius R_0 at the shoot apex (Fig 2-2A).
5. New primordia are formed one by one at a regular time interval, T.
6. The point on M at which the inhibitory field strength is smallest gives the radial position of the formation of a new primordium.
7. Primordia move away from the center of the shoot apex with a radial velocity of $V(r)$ that is proportional to the radial distance r because of the exponential growth of the shoot apex.

At the time when the nth primordium L_n is arising, for a position $(R_0 \cos \theta, R_0 \sin \theta)$ on the circle M, the inhibitory field strength $I(\theta)$ is calculated by summing the inhibitory effects from all preceding primordia, L_1 to L_{n-1}, as follows:

$$I(\theta) \equiv \sum_{m=1}^{n-1} k\big(d_m(\theta)\big)^{-\eta} = k \sum_{m=1}^{n-1} \big(R_0^2 + r_m^2 - 2R_0 r_m \cos(\theta - \theta_m)\big)^{-\frac{\eta}{2}}, \qquad (2-1)$$

where d_m is the distance between the position $(R_0 \cos \theta, R_0 \sin \theta)$ and the mth primordium $(r_m \cos \theta_m, r_m \sin \theta_m)$ and k is a proportional coefficient (Fig 2-2A). In this equation, the inhibitory field

strength is assumed to be inversely proportional to the ηth power of the distance from the point emitting the inhibitory power.

Considering assumptions 5 and 7, the distance from the center of the shoot apex to the mth primordium (r_m) is expressed with the initial radial velocity V_0 as:

$$r_m = R_0 e^{\frac{V_0}{R_0}(n-m)T}. \tag{2-2}$$

The total inhibitory field strength I is expressed as:

$$I(\theta) = \frac{k}{R_0^{\eta}} \sum_{m=1}^{n-1} \left\{ 1 + e^{2(n-m)G} - 2e^{(n-m)G} \cos(\theta - \theta_m) \right\}^{-\frac{\eta}{2}}, \tag{2-3}$$

where G is defined as $G \equiv V_0 T / R_0 = \ln(r_{m+1}/r_m)$. Morphometrically, r_{m+1}/r_m is identical to the "plastochron ratio" introduced by Richards (1951).

The point $(R_0 \cos \theta, R_0 \sin \theta)$ where $I(\theta)$ is smallest is chosen for the position of a new primordium. Note that η and G are the only relevant parameters that influence the behavior of $I(\theta)$ in DC1.

DC2 model

The essential points of the DC2 model are as follows (Douady and Couder, 1996b).

1. The shoot apex is considered as a cone with an apical angle of ψ.
2. Each leaf primordium L emits a constant level of an inhibitory power, which generates an inhibitory field around it.
3. The inhibitory field strength decreases as a function of the distance, d.
4. The formation of new primordia is restricted to the SAM periphery represented by the circle M with a distance of R_0 from the conical vertex.
5. When the inhibitory field strength falls below a given threshold E_s somewhere on M, a new primordium is formed immediately at that point.
6. Primordia move away from the center of the shoot apex with a radial velocity of $V(r)$ that is proportional to the radial distance r because of the exponential growth of the shoot apex.

Positions on the conical surface are expressed in spherical coordinates $\left(r, \frac{\psi}{2}, \theta \right)$ (Fig 2-2B). The inhibitory field strength $I(\theta)$ at the position $\left(R_0, \frac{\psi}{2}, \theta \right)$ on M is calculated by summing the inhibitory effects from all preceding primordia, L_1 to L_{n-1}, as follows:

$$I(\theta) \equiv \sum_{m=1}^{n-1} E \left(\frac{d_m(\theta)}{d_0} \right), \tag{2-4}$$

where d_m is the distance between the mth primordium and the position $\left(R_0, \frac{\psi}{2}, \theta \right)$, d_0 is the maximum distance within which an existing primordium excludes a new primordium, and E is the inhibitory effect

from the preceding primordium, which is defined as a monotonically decreasing, downward-convex function:

$$E(x) \equiv E_s \frac{-1 + (\tanh \alpha x)^{-1}}{-1 + (\tanh \alpha)^{-1}}, \qquad (2-5)$$

where, if $I(\theta) < E_s$, a new primordium is placed at the position $\left(R_0, \frac{\psi}{2}, \theta\right)$. Throughout this study, $E_s = 1$.

Because of assumption 6, the distance from the center of the shoot apex to the mth primordium on the conical surface (r_m) is expressed with the time after its emergence T_m and the initial radial velocity V_0 as:

$$r_m = R_0 e^{\frac{V_0}{R_0}T_m}. \qquad (2-6)$$

By using $t_m \equiv T_m V_0 / R_0$, a standardized age of the mth primordium defined as the product of T_m and the relative SAM growth rate V_0/R_0, r_m is more simply expressed as:

$$r_m = R_0 e^{t_m}. \qquad (2-7)$$

The DC2 model is characterized by three parameters: α, $N \equiv \sin \frac{\psi}{2}$, and $\Gamma \equiv \frac{d_0}{R_0 \sqrt{N}}$. These parameters represent the steepness of the decline of the inhibitory effect around the threshold, the flatness of the shoot apex, and the ratio of the inhibition range to the SAM size, respectively.

In DC2, as a distance between points $\left(r_{(1)}, \frac{\psi}{2}, \theta_{(1)}\right)$ and $\left(r_{(2)}, \frac{\psi}{2}, \theta_{(2)}\right)$ on the conical surface, instead of the true Euclidian distance, its slightly modified version (as defined in the following equation) was used to avoid the discontinuity problem (Douady and Couder 1996b):

$$d \equiv \sqrt{\frac{\left(r_{(1)} - r_{(2)}\right)^2}{N} + 2N r_{(1)} r_{(2)} \{1 - \cos(\theta_{(1)} - \theta_{(2)})\}}. \qquad (2-8)$$

Computer simulation

Model simulations were implemented in C++ with Visual C++ in Microsoft Visual Studio 2015 as an integrated development environment. Contour mapping was performed using OpenCV ver. 3.3.1 (https://opencv.org/).

Computer simulations using DC2 and DC2-derived models were initiated by placing a single primordium or two primordia at a central angle of $120°$ on the SAM periphery. In the former initial condition, the second primordium arises at a certain time or immediately after the first primordium, in dependence on parameter settings, at the opposite position, and in some cases, more primordia are immediately inserted at middle positions. Thus, computer simulations with this condition substantially cover situations starting with 1×2^x primordia $(x = 0, 1, 2, \cdots)$ evenly distributed on the SAM periphery. Similarly, simulations with the latter condition substantially cover situations starting with 3×2^x primordia $(x = 0, 1, 2, \cdots)$. I also tested simulations with another initial condition, in which two primordia were placed at opposite positions with a central angle of $180°$, but they returned completely same results as simulations initiated by placing a single primordium did and are therefore omitted.

Computer simulations were performed with an angle resolution of 0.1°. DC2 and DC2-derived models were simulated with a time step of $\Delta t_{sim} = 0.001$.

In all model simulations, calculation was iterated until the total number of primordia reached 100. For alternate patterns generated by simulation, the last nine primordia were used to judge the stability and regularity of divergence angles. For the other patterns, the last two nodes were used to judge the stability of the number of primordia per node. Then the patterns were categorized and displayed as shown in Fig 2-3.

Results

Morphological characterization of phyllotaxis in *Orixa japonica*

First, I performed an anatomical analysis of the apical winter buds of *O. japonica*, to characterize morphologically its phyllotaxis. In the transverse sections of the winter buds, there was a very obvious tetrastichous pattern of leaf primordia, which were arranged in opposite pairs on either of two orthogonal lines (Fig 2-4A). This pattern looked similar to decussate phyllotaxis; however, unlike decussate phyllotaxis, it was not symmetric. Opposite pairs of primordia varied in size and radial distance and, in each pair, a smaller primordium was positioned closer to the center of the shoot apex. Such asymmetry was also clearly recognized in the longitudinal sections and by observations performed using SEM (Fig 2-4B and 2-4C). Importantly, SEM observations detected incipient primordia that were not paired (Fig 2-4C). Therefore, the asymmetric arrangement of leaves was attributed to the alternate initiation of leaf primordia instead of the secondary displacement of originally decussate leaf primordia. The divergence angle between successive primordia changed in the sequence of approximately $180°$, $90°$, $-180°$ ($180°$), and $-90°$ ($270°$), and this cycle was repeated a few times in the winter bud (Fig 2-4D). These results confirmed that the phyllotaxis of *O. japonica* is genuinely an "orixate phyllotaxis".

Richards' plastochron ratio was found to oscillate in relation to the divergence angle. Plastochron ratios measured from the adjacent pairs of primordia with a divergence angle of approximately $\pm90°$ were significantly larger than those measured from the opposite pairs with a divergence angle of approximately $\pm180°$ (Fig 2-4E). A similar relationship between divergence angles and plastochron ratios had been, albeit fragmentarily, described for orixate phyllotaxis of *K. uvaria* (Snow, 1958); thus, it is likely to be a common feature of orixate phyllotaxis.

Computer simulation assessment of DC1 regarding the ability to produce orixate phyllotactic patterns

DC1 is an inhibitory field model specialized for alternate phyllotactic patterning. DC1 assumes one-by-one formation of leaf primordia at a constant time interval, which strongly limits the model flexibility (Douady and Couder, 1996a). Nevertheless, as this constraint makes the patterning process simple and possible to be dealt with theoretically, it is worth investigating DC1 as a primary model for generation of any types of alternate phyllotaxis.

To test whether DC1 can produce orixate phyllotaxis, I re-examined this established model via detailed computer simulation analysis using exhaustive combinations of the determinant parameters, η and G. As reported previously (Douady and Couder, 1992; 1996a), distichous and relatively major spiral phyllotactic patterns, i.e., alternate patterns with a regular divergence angle near $180°$, a Fibonacci angle ($137.5°$), or a Lucas angle ($99.5°$), were generated as stable patterns over broad ranges of η and G in these simulations (Fig 2-5). Of note, when η and G were set to 1–3 and about 0.2, respectively, tetrastichous patterns were formed that resembled orixate phyllotaxis, as they showed a four-cycle periodic change of the divergence angle in the order of p, q, $-p$, and $-q$ ($-180° \leq p \leq 180°, |p| > |q|$) (Fig 2-5A). In these patterns, however, the larger absolute value of the divergence angle was considerably deviated from $180°$, whereas this

should be very close to 180° in orixate phyllotaxis (Fig 2-5B). These patterns showed nonorthogonal tetrastichy, which is distinct in appearance from the orthogonal tetrastichy of orixate phyllotaxis (Fig 2-5C). Therefore, I concluded that the tetrastichous patterns found in simulations with DC1 are not orixate and that DC1 does not generate the orixate phyllotactic pattern at any parameter setting. The absence of the occurrence of normal orixate phyllotaxis, the divergence angles of which are exactly $\pm 180°$ and $\pm 90°$, in the context of DC1 can be explained analytically (*See Appendix*).

Expansion of DC1 by introducing age-dependent changes in the inhibitory power

Next, I examined whether modification of DC1 could enable it to produce orixate phyllotaxis. In an attempt to modify DC1, I focused on the inhibitory power of each leaf primordium against new primordium formation—which is assumed to be constant in DC models but may possibly change during leaf development—and expanded DC1 by introducing age-dependent, sigmoidal changes in the inhibitory power. In this expanded version of DC1 (EDC1), the inhibitory field strength $I(\theta)$ was redefined as the summation of the products of the age-dependent change in the inhibitory power and the distance-dependent decline of its effect:

$$I(\theta) \equiv \sum_{m=1}^{n-1} \left\{ k\left(d_m(\theta)\right)^{-\eta} F(n-m) \right\}. \tag{2-9}$$

F is defined as:

$$F(\Delta t) \equiv \frac{1}{1 + e^{-a(\Delta t - b)}}, \tag{2-10}$$

where parameters a and b are constants that represent the rate and timing of the age-dependent changes in the inhibitory power, respectively. Under this equation, in an age-dependent manner, the inhibitory power increases at $a > 0$ and decreases at $a < 0$. In the present study, η was fixed at 2 for EDC1.

Prior to computer simulation analysis with EDC1, I searched for parameters of EDC1 that can fit the requirements of normal orixate phyllotaxis. When the normal pattern of orixate phyllotaxis is stably maintained, a rectangular coordinate system with the origin at the center of the shoot apex can be set such that all primordia lie on the coordinate axes, and every fourth primordium is located on the same axis in the same direction, i.e., the position of any primordium (m^{th} primordium) can be expressed as $(r_m \cos\theta_{m-4i}, r_m \sin\theta_{m-4i})$ for integers i. Under this condition, I considered whether a new primordium (n^{th} primordium) is produced at the position $(R_0 \cos\theta_{n-4i}, R_0 \sin\theta_{n-4i})$, to keep the normal orixate phyllotactic pattern. In EDC1, as in DC1, new primordium formation at $(R_0 \cos\theta_{n-4i}, R_0 \sin\theta_{n-4i})$ implies that the inhibitory field strength $I(\theta)$ on the circle M has a minimum at θ_{n-4i}. For this reason, I first attempted to solve the following equation:

$$\left. \frac{dI(\theta)}{d\theta} \right|_{\theta - \theta_{n-4i}=0} = 0. \tag{2-11}$$

This equation was numerically solved under two geometrical situations of primordia: the divergence angle between the newly arising primordium and the last primordium is $\pm 90°$ (situation 1) or $\pm 180°$ (situation 2)

(Fig 2-6A). The solutions obtained identified parameter sets that satisfied the above equation under both these two situations (Figs 2-6B and 2-7B). The calculation of $I(\theta)$ using the identified parameter sets showed that $I(\theta)$ has a local and global minimum around θ_{n-4i} with large values of G, such as 0.5 or 1, while it has a local maximum instead of a minimum around θ_{n-4i} with small G values, such as 0.1 (Fig 2-6C). This result indicates the possibility that EDC1 can form orixate phyllotaxis as a stable pattern under a particular parameter setting with large G values.

Generation of orixate phyllotactic patterns in a computer simulation using EDC1

I conducted computer simulations using EDC1 over broad ranges of parameters and found that EDC1 could generate tetrastichous alternate patterns in addition to distichous and spiral patterns (Fig 2-7B). The tetrastichous patterns included orthogonal tetrastichous ones with a four-cycle divergence angle change of approximately 180°, 90°, −180°, and −90°, which can be regarded as orixate phyllotaxis (Figs 2-7C and 2-8). Under the conditions of assuming an age-dependent increase in the inhibitory power ($a > 0$), these orixate patterns were formed within a rather narrow parameter range of $G = 0.5{\sim}1$, $a = 1{\sim}2$, and $b = 4{\sim}9$ around the parameter settings that were determined by numerical solution, to fit the requirements for the stable maintenance of normal orixate phyllotaxis (Fig 2-7B and 2-7C). When assuming an age-dependent decrease in the inhibitory power ($a < 0$), orixate phyllotaxis appeared at a point of $G = 0.1$, $a \approx -10$, and $b \approx 3.5$ (Fig 2-7B and 2-7C). These values of a and b represent a very sharp drop in the inhibitory power at the primordial age corresponding to approximately three plastochron units. Around this parameter condition, there were no numerical solutions for normal orixate phyllotaxis; however, patterns that were substantially orixate, although they were not completely normal, could be established. The orixate patterns that were generated under the conditions in which the inhibitory power increased and decreased were visually characterized by sparse primordia around the small meristem and dense primordia around the large meristem, respectively (Fig 2-7C).

In the results of computer simulations with EDC1, besides the orixate patterns, I also found peculiar patterns with an x-cycle change in the divergence angle consisting of 180° followed by an $(x - 1)$-times repeat of 0° (Fig 2-9). Such patterns were generated when all the parameters a, b, and G were set to relatively large values and are displayed as periodic distribution of black regions in the upper right area of the middle and right panels of Fig 2-7B. In these patterns, as b is increased, the number of repetition times of 0° is increased, resulting in the shift from x-cycle to $(x + 1)$-cycle. This shift is mediated by the occurrence of spiral patterns with a small divergence angle, and the transitions from x-cycle to spiral and from spiral to $(x + 1)$-cycle takes place suddenly in response to a slight change of b (Fig 2-9).

Computer simulation assessment of DC2 regarding the ability of producing orixate phyllotactic patterns

DC2, as DC1, is an inhibitory field model but is more generalized than DC1 (Douady and Couder, 1996b). Unlike DC1, DC2 does not assume one-by-one formation of primordia at a constant time interval and thus does not exclude whorled phyllotactic patterning. Indeed, DC2 was shown to produce all major patterns of

either alternate or whorled phyllotaxis depending on parameter conditions (Douady and Couder, 1996b). To test whether DC2 can generate orixate phyllotactic patterns, I carried out extensive computer simulation analyses using this model. My computer simulations confirmed that major phyllotactic patterns, such as distichous, Fibonacci spiral, Lucas spiral, decussate, and tricussate patterns, are formed as stable patterns in wide ranges of parameters, and also showed formation of tetrastichous alternate patterns with a four-cycle change of the divergence angle at $N = 1$ and $\Gamma \approx 1.8$ when initiated by placing a single primordium at the SAM periphery (Fig 2-10A). The possible inclusion of orixate phyllotaxis in these tetrastichous four-cycle patterns was carefully examined based on the ratio of plastochron times and the ratio of absolute values of divergence angles, which should be much larger than 0 and close to 0.5, respectively, in orixate phyllotaxis. Although all the tetrastichous four-cycle patterns detected here had a divergence angle ratio near 0.5, their ratios of plastochron times were too small to be regarded as orixate phyllotaxis, and the overall characters indicated that they are rather similar to decussate phyllotaxis (Fig 2-10B and 2-10C). These results led to the conclusion that the DC2 system does not generate orixate phyllotaxis under any parameter conditions.

Expansion of DC2 by introducing age-dependent changes in the inhibitory power

Similar to the approach used for DC1, I expanded DC2 by introducing primordial age-dependent changes in the inhibitory power. In this expanded version of DC2 (EDC2), the inhibitory field strength $I(\theta)$ was redefined as the summation of the products of the age-dependent change in the inhibitory power and the distance-dependent decrease of its effect:

$$I(\theta) \equiv \sum_{m=1}^{n-1} \left\{ E\left(\frac{d_m(\theta)}{d_0}\right) F(t_m) \right\}, \qquad (2-12)$$

where F is a function expressing a temporal change in the inhibitory power, defined as:

$$F(t) \equiv \frac{1}{1 + e^{-A(t-B)}}. \qquad (2-13)$$

Generation of orixate phyllotactic patterns in a computer simulation using EDC2

Computer simulations using EDC2 were first conducted under a wide range of combinations of A and B at three different settings of Γ ($\Gamma = 1, 2, \text{or } 3$) and fixed conditions for α and N ($\alpha = 1, N = 1/3$) (Fig 2-11). In this analysis, tetrastichous four-cycle patterns were formed within the parameter window where A was 3–7 and B was 0.4–1, which represents a late and slow increase in the inhibitory power during primordium development (Fig 2-12A). Further analysis performed by changing Γ, α, and N showed that small values of α, which indicate that the distance-dependent decrease in the inhibitory effect is gradual, and large values of Γ, which indicate that the maximum inhibition range of a primordium is large, are also important for the formation of tetrastichous four-cycle patterns (Figs 2-13 and 2-14). All of these four-cycle patterns were found to be almost orthogonal and to have a sufficiently large ratio of successive plastochron times, thus fitting the criterion of orixate phyllotaxis (Figs 2-12B and 2-15). Furthermore, the plots of these patterns lied within the cloud of the data points of real orixate phyllotaxis, and therefore I concluded that they are orixate. A typical

example of such orixate patterns was obtained by simulation using the parameters, $A = 4.8$, $B = 0.72$, $\Gamma = 2.8$, $N = 1/3$, and $\alpha = 1$, and is presented as a contour map of the inhibitory field strength in Fig 2-16A, which clearly depicts orixate phyllotactic patterning. Under this parameter condition, the inhibitory field strength on the SAM periphery was calculated to have a minimum close to the threshold at $0°$ at the time of new primordium formation when the preceding primordia were placed at $0°$, $180°$, and $\pm90°$ (Fig 2-17). This landscape of the inhibitory field stabilizes the orixate arrangement of primordia. In summary, my analysis demonstrated that orixate phyllotaxis comes into existence in the EDC2 system when the inhibitory power of each primordium increases at a late stage and slowly to a large maximum and when its effect decreases gradually with distance.

In the orixate phyllotactic patterns generated by EDC2, the plastochron time oscillated between two values together with a cyclic change in the divergence angle: the longer plastochron was observed for the adjacent pairs of primordia with a divergence angle of $\pm90°$ and the shorter plastochron was recorded for the opposite pairs with a divergence angle of $\pm180°$ (Fig 2-16B). This relationship between the plastochron and the divergence angle agreed with the real linkage observed for the plastochron ratios and divergence angles in the winter buds of *O. japonica* (Fig 2-4E).

Distribution of phyllotactic patterns in the parameter space of EDC2

Based on a comprehensive survey of the results of the computer simulations performed using EDC2, I examined the distribution of various phyllotactic patterns and the possible relationships between them in the parameter space of EDC2 (Figs 2-11, 2-12A, 2-13, 2-14, 2-18, 2-19). Major phyllotactic patterns, such as the distichous, Fibonacci spiral, and decussate patterns, occupied large areas in the parameter space, and the Lucas spiral pattern occupied some areas. Depending on the initial condition, the tricussate pattern also took a considerable fraction of the space. In the parameter space, the distichous pattern adjoined the Fibonacci spiral pattern, while the Fibonacci spiral adjoined the distichous, Lucas spiral, decussate, and tricussate patterns. The regions where the orixate pattern was generated were located next to the regions of the decussate, Fibonacci spiral, Lucas spiral, and/or two-cycle alternate patterns. This positional relationship suggests that orixate phyllotaxis is more closely related to the decussate and spiral patterns than it is to the distichous pattern. The two-cycle patterns formed in a narrow parameter space next to the region of orixate phyllotaxis and had a divergence angle ratio of approximately 0.55 and a plastochron time ratio of approximately 0.2 (Figs 2-12B and 2-20A); thus, they are similar to semi-decussate phyllotaxis, which is an alternate arrangement characterized by the oscillation of the divergence angle between 180° and 90° (Fig 2-20B). These semi-decussate-like patterns were not observed in the computer simulations performed using DC2 (Fig 2-10B and 2-10C); rather, they were produced only after its expansion into EDC2.

The overall distributions of major phyllotactic patterns in the parameter space were compared between DC2 and EDC2 using color plots drawn from the results of simulations conducted for EDC2 with various settings of the inhibition range parameter Γ and the inhibitory power change parameter A (Fig 2-13). In these simulations, large A values accelerated the age-dependent increase in the inhibitory power of each primordium; if A is sufficiently large, the inhibitory power is almost constant during primordium

development and the EDC2 system is almost the same as DC2. Therefore, the colors along the top side of each panel of Fig 2-13, where A was set to 20, which is a high value, show the phyllotactic pattern distribution against Γ in DC2, while the colors over the two-dimensional panel show the phyllotactic pattern distribution against Γ and A in EDC2. The order of distribution of the distichous, Fibonacci spiral, and decussate patterns was unaffected by decreasing A and, thus, did not differ between DC2 and EDC2. As reported in the previous study of DC2 (Douady and Couder, 1996b), on the top side of Fig 2-13, the stable pattern changed from distichous to Fibonacci spiral, and then turned into decussate as Γ decreased. In the parameter space of EDC2, this order of distribution of major phyllotactic patterns was not affected much by decreasing A to moderate values; however, when A was further decreased, the orixate pattern appeared in the region of the Fibonacci spiral (Figs 2-13 and 2-19). As A decreased, the range of Γ that produced a Fibonacci spiral became wider and the transition zone between the distichous and Fibonacci spiral patterns, where the divergence angle gradually changed from 180° to 137.5°, became narrower (Fig 2-13). This result indicated that Fibonacci spiral phyllotaxis is more dominant when assuming a delay in the primordial age-dependent increase in the inhibitory power.

Discussion

Orixate phyllotaxis is a special kind of alternate phyllotaxis with orthogonal tetrastichy resulting from a four-cycle change in the divergence angle in the order of approximately 180°, 90°, −180° (180°), and −90° (270°); this phyllotaxis occurs in a few plant species across distant taxa (Maekawa, 1948; Berger, 1908; Troll, 1937; Snow, 1958). In the present study, I investigated a possible theoretical framework behind this minor but interesting phyllotaxis on the basis of the inhibitory field models proposed by Douady and Couder (Douady and Couder, 1996a; 1996b), which were shown to give a simple and robust explanation for the self-organization process of major phyllotactic patterns by assuming that each existing leaf primordium emits a constant level of inhibitory power against the formation of a new primordium and that its effect decreases with distance from the primordium. Re-examination of the original versions of Douady and Couder's models (DC1 and DC2) via exhaustive computer simulations revealed that they do not generate the orixate pattern at any parameter condition. The inability of DC models to produce orixate phyllotaxis prompted me to expand them to account for a more comprehensive generation of phyllotactic patterns. In an attempt to modify DC models, I introduced a temporal change in the inhibitory power during primordium development, instead of using a constant inhibitory power. Such changes of the inhibitory power were partly considered in several previous studies. Douady and Couder assessed the effects of "the growth of the element's size", which is equivalent to the primordial age-dependent increase in the inhibitory power and found that it stabilizes whorled phyllotactic patterns (Douady and Couder, 1996b). Smith et al. assumed in their mathematical model that the inhibitory power of each primordium decays exponentially with age and stated that this decay promoted phyllotactic pattern formation de novo, as well as pattern transition, and allowed the maintenance of patterns for wider ranges of parameters (Smith et al., 2006b). A DC1-based model equipped with a primordial age-dependent change in the inhibitory power was also used to investigate floral organ arrangement (Kitazawa and Fujimoto, 2015; 2018). In these studies, however, temporal changes in the inhibitory power were examined under limited ranges of parameters focusing on particular aspects of phyllotactic patterning, and the possibility of the generation of minor patterns, such as orixate phyllotaxis, was not addressed.

I expanded DC1 into EDC1 and DC2 into EDC2 by simply incorporating the assumption that the inhibitory power of a primordium is not necessarily constant but may increase or decrease sigmoidally with its age. Extensive computer simulations performed using EDC1 and EDC2 over wide ranges of parameters demonstrated that both of the expanded models can produce orixate phyllotaxis under some parameter conditions. In EDC1, orixate patterns occurred when the inhibitory power was set to increase gradually at large values of the parameter G, which represent a small SAM relative to the growth velocity and/or plastochron, and when the inhibitory power decreased suddenly after a certain time lag of about $3T$ at small G values, which represent a large SAM. In these two conditions, orixate phyllotactic patterns obviously arise for distinct reasons (Fig 2-21). Here, let me consider the effect of four pre-existing primordia, which are arranged in the normal orixate pattern on the orthogonal tetrastichy lines, on a new primordium arising at 0°. The key requirements for the formation of a new primordium at 0° to maintain the orixate pattern are: that

the inhibitory effects of the primordia at $\pm 90°$ (previous and second or third previous primordia) are balanced at the site of new primordium formation, and that the inhibitory effect from the fourth previous primordium at $0°$ is negligible. In the case of a large G value with a gradual increase in the inhibitory power, the primordia at $\pm 90°$ are quite different in the distance to the new primordium site, but their effect can be equalized because of the compensation of the distance-dependent decrease in the inhibitory effect by the age-dependent increase in the inhibitory power, and the fourth previous primordium has little impact because it is located far away. In contrast, in the case of a small G value with a sudden decrease in the inhibitory power, the primordia at $\pm 90°$ exhibit almost the same distance and, therefore, almost the same strength of influence on the site of formation of the new primordium, and the fourth previous primordium no longer has an impact because of the immediately preceding sharp drop in its inhibitory power.

In EDC2, the constraint imposed in EDC1 that leaf primordia are formed one by one at a regular time interval is removed, which allows the simultaneous formation of two or more primordia. Probably because the removal of this constraint destabilizes orixate patterning with a sudden decrease in the inhibitory power, EDC2, unlike EDC1, generated orixate phyllotaxis as a stable pattern only when the inhibitory power was assumed to increase at a late stage and slowly. The orixate patterns produced using EDC2 under this condition had relatively small and large plastochron ratios for the opposite and adjacent pairs of primordia, respectively. A similar feature was observed in the phyllotactic pattern of the winter buds of *O. japonica* and was previously reported for the orixate phyllotactic patterns of *Kniphofia* (Snow, 1958). These findings suggest that orixate pattern generation in computer simulations performed using EDC2 reflects actual phyllotaxis development and that the occurrence of orixate phyllotaxis in distant plant species can be generally explained by the slow and late increase in the inhibitory power. In real plants, the first leaf primordium arises under some influence of pre-existing structures such as cotyledons, which should be considered as the initial condition in model simulation analysis. However, as simulations with EDC2 under two different initial conditions produced orixate patterns at similar parameter settings, orixate phyllotaxis seems not to require specific initial conditions.

There are two views regarding the relationship between orixate phyllotaxis and major phyllotactic patterns. One view was derived from ontogenic observations and regards orixate phyllotaxis as an intermediate form between the distichous and decussate patterns (Maekawa, 1948), while the other view was derived from a theoretical consideration of symmetry-breaking processes and regards orixate phyllotaxis as an intermediate form between the spiral and decussate patterns (Yamada et al., 2004). In the parameter space of EDC2, orixate patterns were located in the vicinities of the regions of the decussate, Fibonacci spiral, and Lucas spiral patterns, which indicates a close relationship between orixate phyllotaxis and the decussate and spiral patterns, but not the distichous phyllotaxis; thus, this observation favors the latter view. Among the neighbors of orixate phyllotaxis, oscillating patterns were also found, including a semi-decussate-like one, which could not be generated in DC2. Semi-decussate or semi-decussate-like phyllotaxis is quite rare in nature and has been described in only a few plants, such as *Najas guadalupensis* and *Kniphofia* "Tubergeniana" (Bereger, 1908; Troll, 1937; Snow, 1958). The tomato plant (*Solanum lycopersicum*) Shin-Toyotama No. 2, a Japanese cultivar, and *e-2*, a mutant of *Sister-of-PIN1*, which is a paralogue of the auxin-efflux carrier gene *PIN1*, were also

reported to exhibit a semi-decussate pattern (Usugami, 1964; Martinez et al., 2016). Among these plants, *K.* "Tubergeniana" is of particular interest, because its relatives of the same genus have orixate phyllotaxis (*K. uvaria*, *K. pumila*, and *K. tysonii*) or spiral phyllotaxis (*K. northiae*) (Berger, 1908; Snow, 1958). This phyllotactic variety in *Kniphofia* fits well the simulation result that the spiral and semi-decussate-like patterns were located close to the orixate pattern in the EDC2 parameter space and can be converted into the orixate pattern by small changes in the parameters.

The Fibonacci spiral with a divergence angle close to the golden angle (137.5°) is one of the most common patterns of phyllotaxis observed in plants and is predominant among the spiral phyllotactic patterns. Although this pattern can be generated by previous inhibitory field models, such as DC models, its dominance has not been fully explained by these models (Okabe, 2016). For example, in DC2, the divergence angle of alternate phyllotaxis is shifted gradually from 180° (distichous) to 137.5° (Fibonacci spiral) as the parameter Γ is reduced from 2.6 to 1.9 at $\alpha = 8$ and $N = 1/3$, and the range of Γ that generates the Fibonacci spiral is not wider than that observed for the other spirals (Fujita, 1939; Douady and Couder, 1996b). My computer simulations performed using EDC2 showed that, compared with DC2, the expanded model assigns a smaller area to spiral patterns with a non-golden angle in the parameter space. This tendency in EDC2 suggests that the dominant occurrence of the golden spiral in nature may be better explained by introducing primordial age-dependent changes in the inhibitory power into the inhibitory field model. In summary, I here propose EDC2 as a more appropriate abstract model of phyllotaxis that can generate a wide range of phyllotactic patterns, including not only major types of phyllotaxis but also orixate and semi-decussate patterns, with reasonable proportions comparable to the frequencies of their natural occurrence.
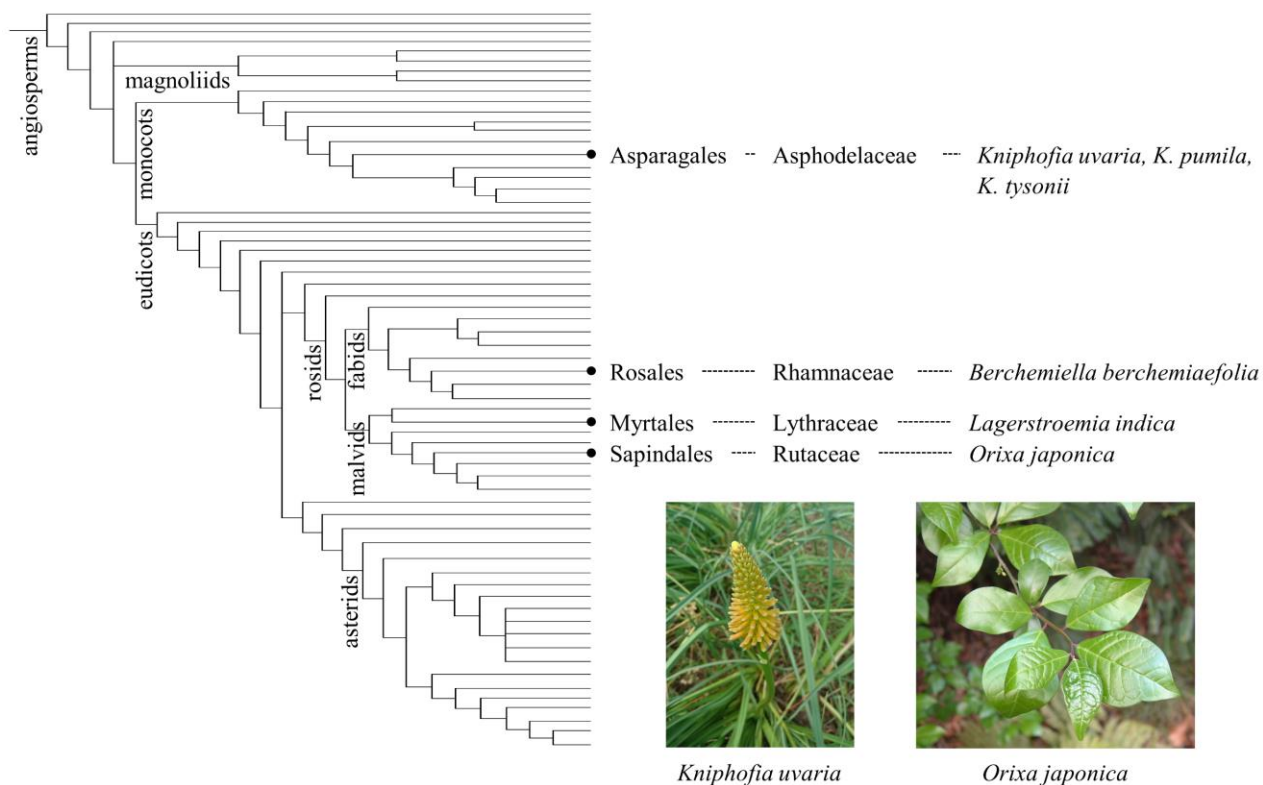
Fig 2-1. Occurrence of plants with orixate phyllotaxis in the angiosperm phylogeny

Plants with orixate phyllotaxis and their positions in the order-level phylogenetic tree of angiosperms based on Angiosperm Phylogeny Poster (Cole et al., 2019).

Fig 2-2. Schematic views of the shoot apex with coordinates in DC models

The shoot apex is considered as a plane in DC1 (A) and as a cone in DC2 (B).

Alternate with a constant divergence angle or a 2-cycle change in the divergence angle

(mean) divergence angle

135°

180°

plastochron time ratio

0°
1

0

1

0

1

divergence angle ratio

99.5°

90°

120°

③

137.5°

60°

150°

②

30°

④

180° ①

0°

1.0   0.5   0.0   0.5   1.0

plastochron time ratio

1.0   ④

Spiral (135°)

0.5

0.0

1.0   0.5   0.0

divergence angle ratio

Tetrastichous alternate with a 4-cycle change in the divergence angle

plastochron time ratio

1.0   ⑥

⑦

0.5

0.0

1.0   0.5   0.0

|divergence angle| ratio

Whorled

⑤

decussate

⑧

tricussate

other whorled

Others

① distichous

② spiral (Fibonacci)

③ spiral (Lucas)

④ semi-decussate

⑤ decussate

⑥ orixate

⑦ orixate

⑧ tricussate

Fig 2-3. Color legend for the phyllotactic patterns generated in computer simulations
The phyllotactic patterns generated in computer simulations were classified into an alternate pattern with a constant divergence angle or a two-cycle change in the divergence angle; a tetrastichous alternate pattern with a four-cycle change in the divergence angle; a whorled pattern; and other patterns. Whorled patterns were further classified into decussate ("opposite phyllotaxis" typified by true decussate), tricussate, and other whorled patterns. These patterns were distinguished using different colors. For regular alternate patterns with a constant divergence angle, the divergence angle was indicated by a color hue from cyan (0°) to red (180°). In the case of alternate patterns with a two-cycle divergence angle change, the color hue was assigned for the mean value of the successive divergence angles. In these two-cycle alternate patterns, small-to-large ratios of two successive plastochron times and two successive divergence angles were represented by lightness (full lightness for 0) and saturation (full saturation for 1), respectively. Tetrastichous alternate patterns with a four-cycle divergence angle change were similarly expressed by color brightness and saturation based on their ratios of plastochron times and divergence angles; however, instead of the divergence angles themselves, the absolute values of divergence angles were used to calculate the ratio of divergence angles. As the divergence angle of this type of alternate pattern changes in the sequence of p, q, $-p$, and $-q$ ($-180° < p, q \leq 180°$), $|q|/|p|$ gives the ratio of the absolute values of divergence angles if $|p| > |q|$. Typical examples of phyllotactic patterns are marked with circled numbers in the color legend and their schematic diagrams are shown at the bottom.
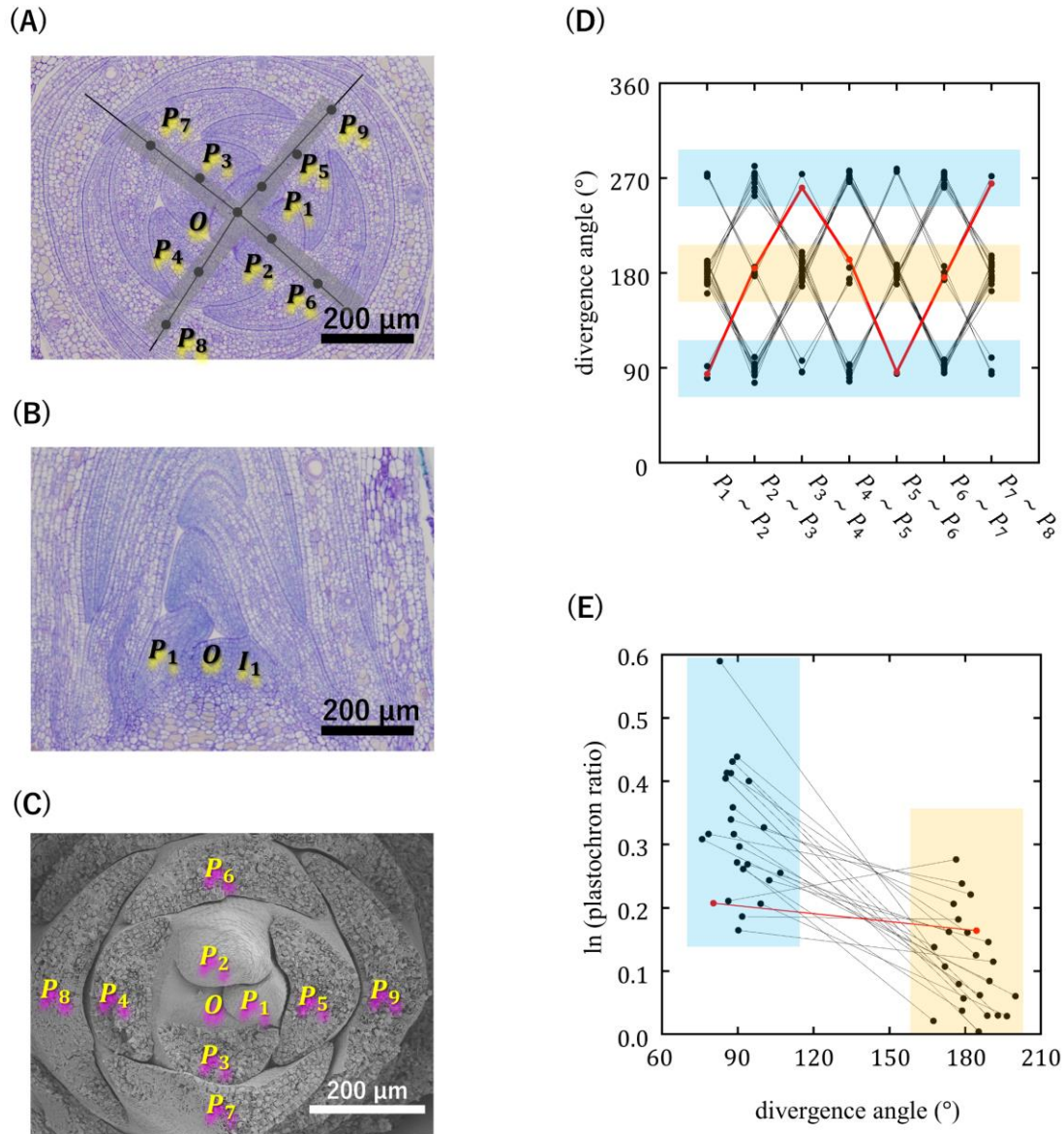
Fig 2-4. Orixate phyllotaxis in the apical winter buds of *Orixa japonica*

(A) Transverse section. O points to the summit of the SAM, and leaf primordia are designated as P_1, P_2, P_3, etc., with P_1 being the youngest visible primordium. Black lines represent orthostichies drawn by joining the gravity centers of leaf primorida and O. The four orthostichy lines can be roughly approximated by two orthogonal lines (pale gray broad lines). (B) Longitudinal section. I_1 indicates the incipient primordium. (C) Scanning electron microscopic image. (D) Divergence angles measured using the transverse sections. Divergence angles close to 180° show opposite positioning of the successive primordia (blue), while angles near 90° or 270° show adjacent positioning (yellow). (E) The natural logs of plastochron ratios OP_2/OP_1 and OP_3/OP_2 are plotted based on whether the two primordia are located in an adjacent or opposite position. In (D) and (E), points linked by a line represent data from the same sample, and red points indicate data obtained from the section of (A).
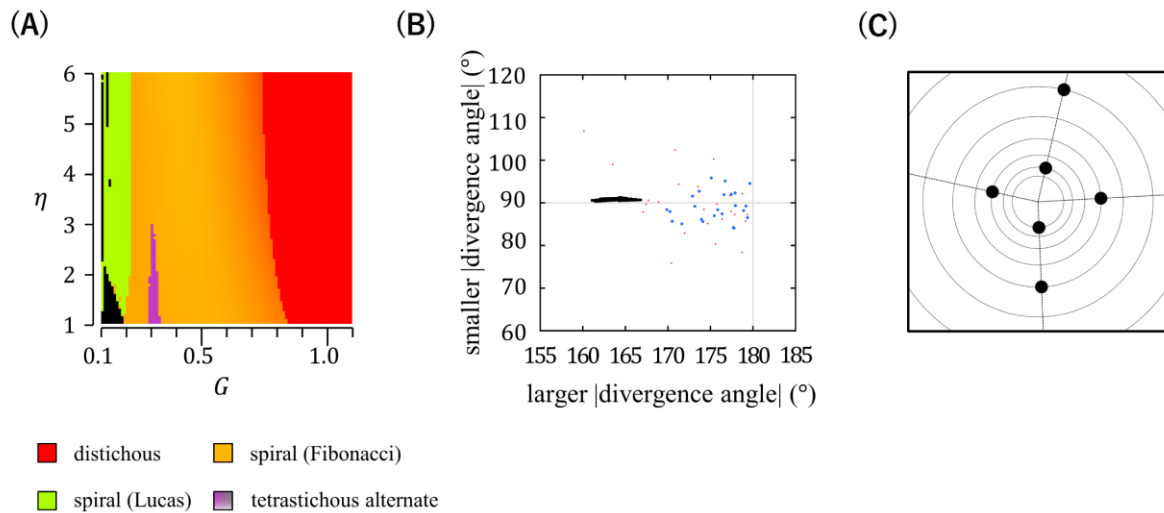
Fig 2-5. Phyllotactic patterns generated in computer simulations using DC1

(A) Computer simulations using DC1 were performed under various settings of parameters G and η (101×101 conditions), and the patterns obtained are displayed according to the color legend shown in Fig 2-3. (B) The black and red dots indicate the absolute values of divergence angles of the tetrastichous alternate patterns generated in (A) and real orixate phyllotaxis observed for winter buds of *O. japonica* (data of $P_1 \sim P_2$ and $P_2 \sim P_3$ in Fig 2-4D), respectively. The blue dots show the averages determined from the real data of $P_1 \sim P_2$ to $P_6 \sim P_7$ (Fig 2-4D) for each winter bud of *O. japonica*. In this panel, alternate patterns with a four-cycle change in divergence angles in the sequence of p, q, $-p$, and $-q$ ($|p| > |q|$) were plotted at the point ($|p|$, $|q|$). (C) An example of the tetrastichous alternate patterns, which was produced by computer simulation at $G = 0.3$ and $\eta = 1.5$. This pattern has a divergence angle change in the sequence of 165°, −91°, −165°, and 91° and, unlike orixate phyllotaxis, exhibits a distorted tetrastichy, rather than an orthogonal tetrastichy.

37

(A)

situation 1   situation 2

(B)

(C)
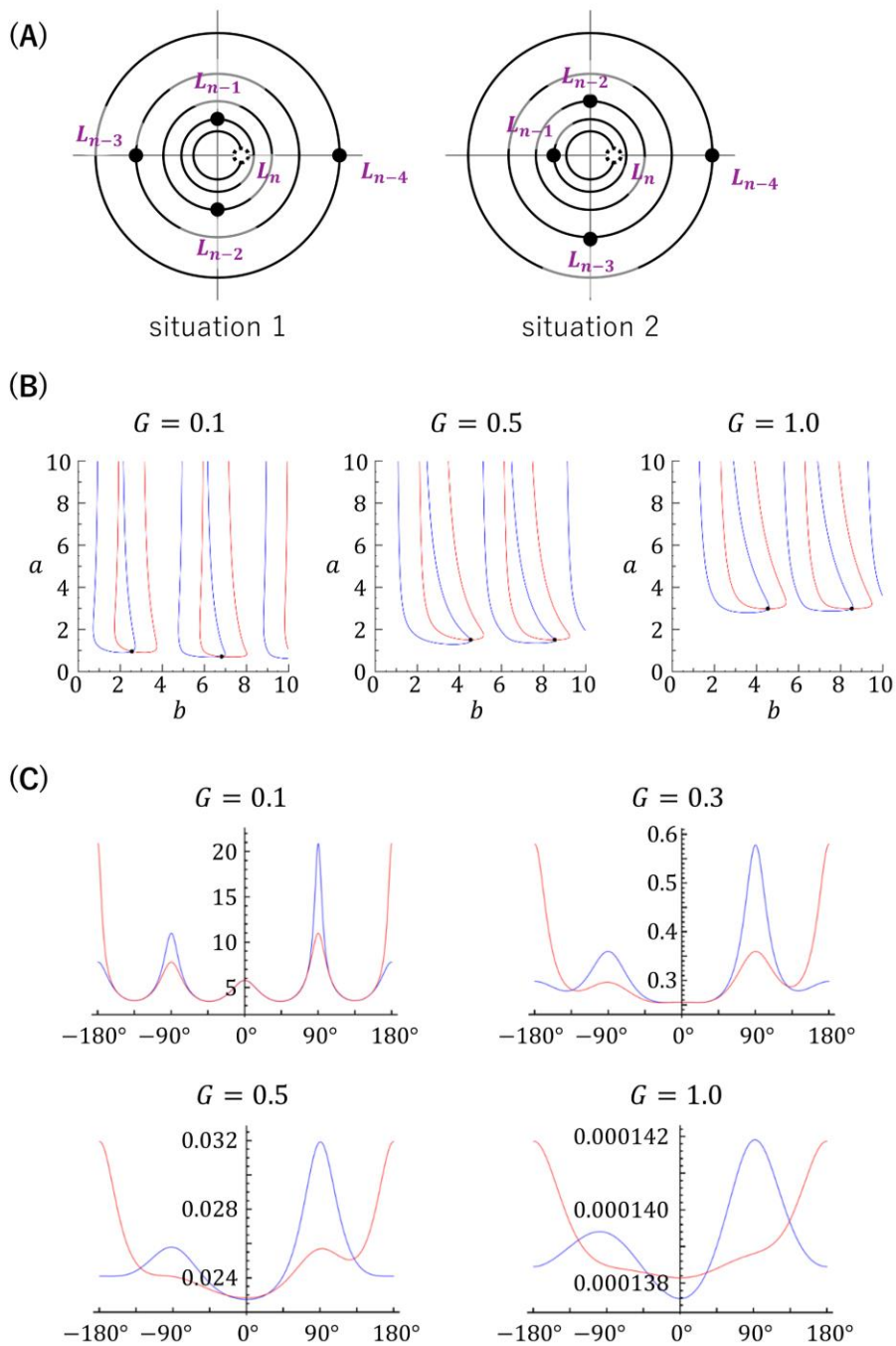
Fig 2-6. Mathematical analysis of the conditions required for normal orixate phyllotaxis in EDC1

(A) Two different situations of the arrangement of the four preceding primordia, L_{n-4}, L_{n-3}, L_{n-2}, and L_{n-1}, relative to the incipient primordium L_n in normal orixate phyllotaxis. (B) The blue and red curves show numerical solutions of $\frac{dI(\theta)}{d\theta}\Big|_{\theta-\theta_{n-4i}=0} = 0$ in situations 1 and 2, respectively. Their intersection points are expected to give the parameter conditions of EDC1 that are required for stabilizing the normal orixate phyllotaxis. (C) Inhibitory field strength on the periphery of SAM in situation 1 (blue) and situation 2 (red) at the parameter settings determined as solutions of $\frac{dI(\theta)}{d\theta}\Big|_{\theta-\theta_{n-4i}=0} = 0$ that are common to both of these situations. Graphs were drawn with θ_{n-4i} as $0°$.

(A)

(B)

distichous

spiral (Fibonacci)

spiral (Lucas)

tetrastichous alternate

(C)
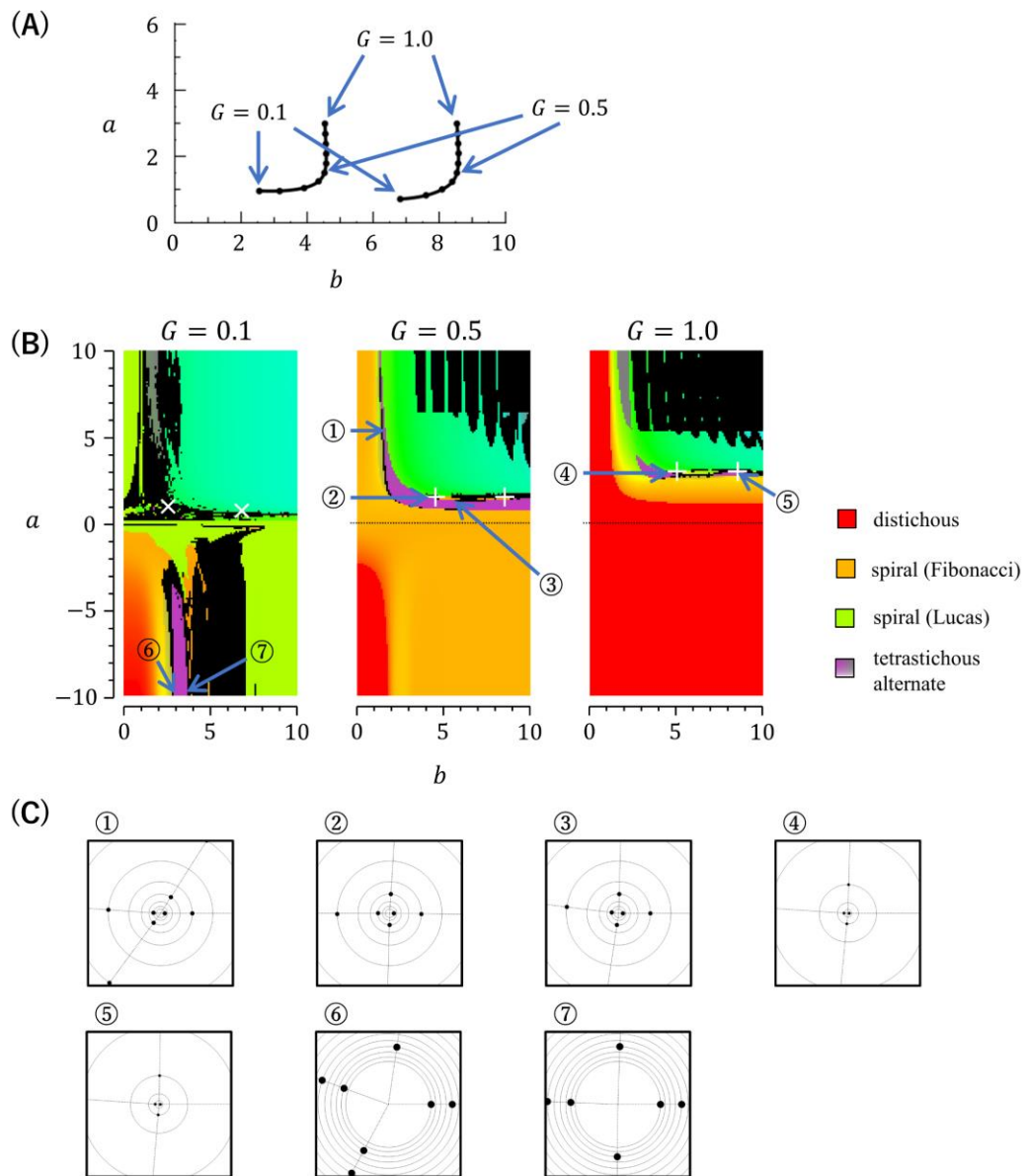
Fig 2-7. Mathematical and computer simulation analysis of EDC1

(A) Numerical solutions of parameters that fit the mathematical requirements for normal orixate phyllotaxis in EDC1. The two curves show the solutions obtained using various G values. The closed circles indicate the solutions obtained with G set at 0.1 intervals between 0.1 and 1.0. (B) Stable patterns generated in computer simulations using EDC1 under various parameter settings (201 settings for a, 101 settings for b, 3 settings for G, and thus $201 \times 101 \times 3 = 60{,}903$ simulations in total). The patterns obtained are displayed according to the color legend shown in Fig 3. The white crosses (+) indicate the parameter conditions obtained as numerical solutions of $\left.\frac{dI(\theta)}{d\theta}\right|_{\theta-\theta_{n-4i}=0} = 0$, giving a minimum of $I(\theta)$ around θ_{n-4i} for normal orixate phyllotaxis, whereas white saltires (×) indicate the parameter conditions obtained as numerical solutions of $\left.\frac{dI(\theta)}{d\theta}\right|_{\theta-\theta_{n-4i}=0} = 0$, giving a maximum of $I(\theta)$. (C) Schematic diagrams of typical examples of the phyllotactic patterns generated in the computer simulations. The circled numbers relate the diagrams to the parameter conditions shown in (B).
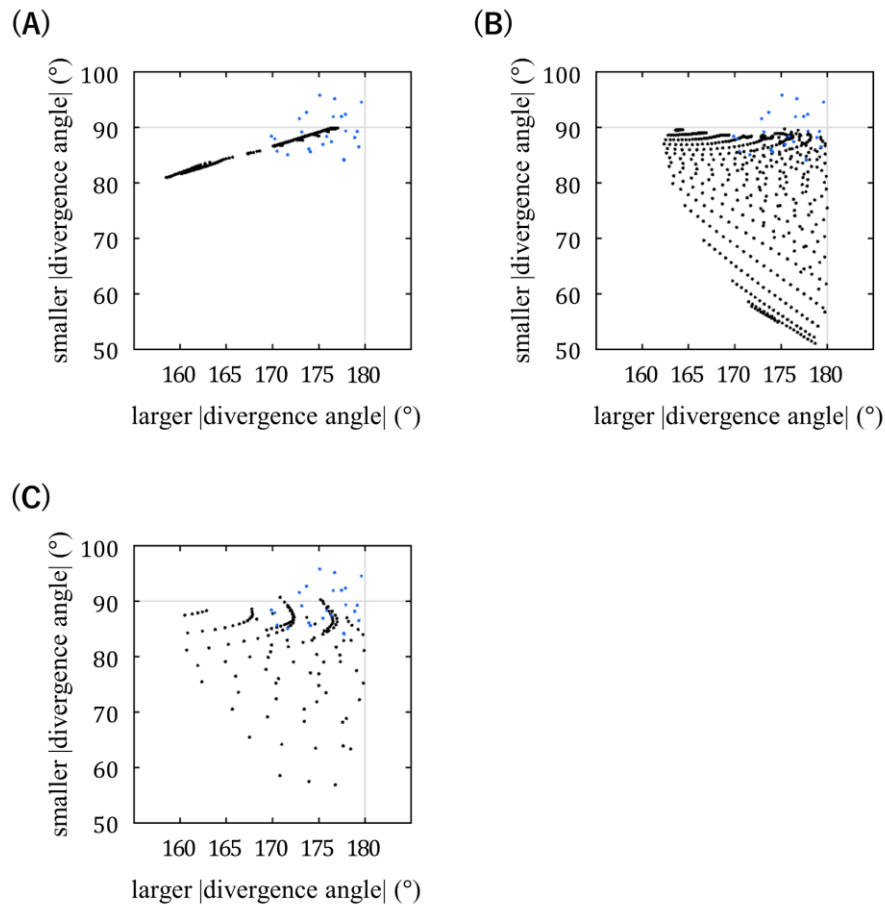
Fig 2-8. Divergence angles of the tetrastichous alternate patterns generated in computer simulations using EDC1

For tetrastichous alternate patterns with a four-cycle change in the divergence angle generated in computer simulations using EDC1 under the conditions of $G = 0.1$ and $a < 0$ (A), $G = 0.5$ and $a > 0$ (B), and $G = 1$ and $a > 0$ (C), the absolute values of divergence angles were plotted using the larger value as the abscissa and the smaller value as the ordinate, such that a pattern with a divergence angle change in the sequence of p, q, $-p$, and $-q$ ($|p| > |q|$) was represented by a black dot at the position $(|p|, |q|)$. The blue dots show the averages determined from the real data of $P_1{\sim}P_2$ to $P_6{\sim}P_7$ (Fig 2-4D) for each winter bud of *O. japonica*.
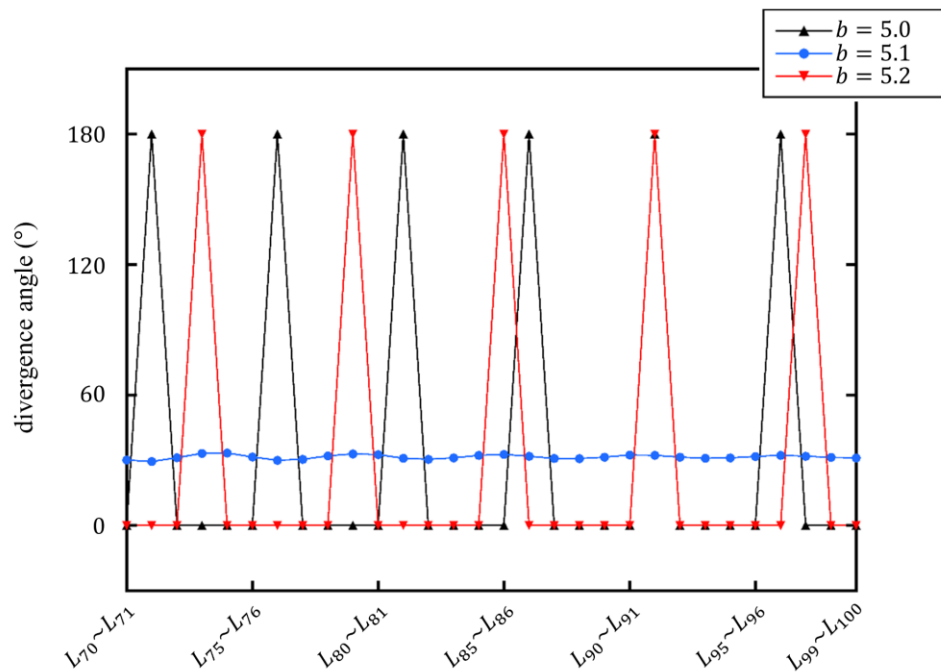
Fig 2-9. Transitions of phyllotactic patterns by a slight increase of b in the computer simulation with EDC1

Computer simulations with EDC1 were performed under the parameter condition of $G = 0.5$, $a = 10$, and $b = 5$, 5.1, or 5.2. Changes in the divergence angle from $L_{70} \sim L_{71}$ to $L_{99} \sim L_{100}$ are shown for the resultant patterns. A small-angle spiral was obtained at $b = 5.1$ (blue circle), while five-cycle and six-cycle alternate patterns were produced at $b = 5$ and at $b = 5.2$, respectively.

(A)

$N = 1/1$ $N = 1/3$

Initiated with a single primordium

Initiated with two primordia

- distichous
- spiral (Fibonacci)
- spiral (Lucas)
- two-cycle alternate
- tetrastichous alternate
- decussate
- tricussate
- tetracussate

(B)

(C)
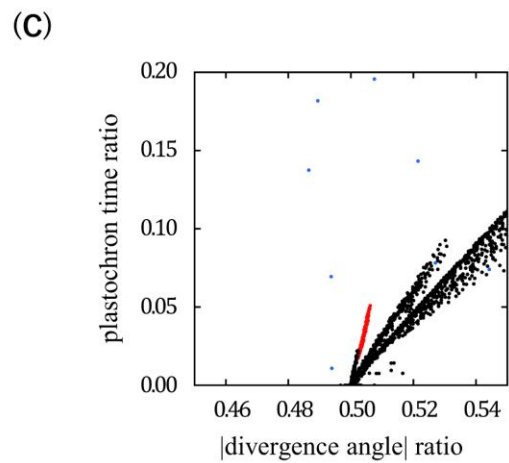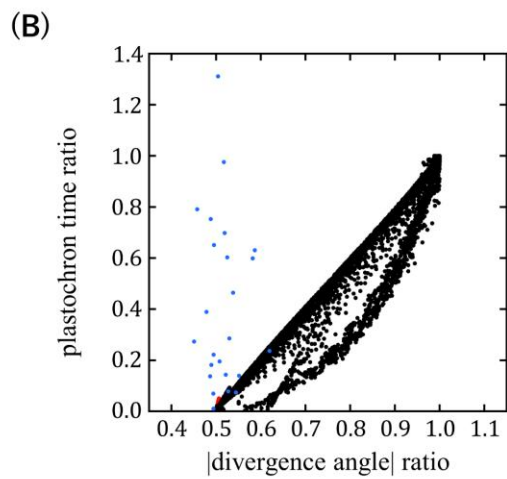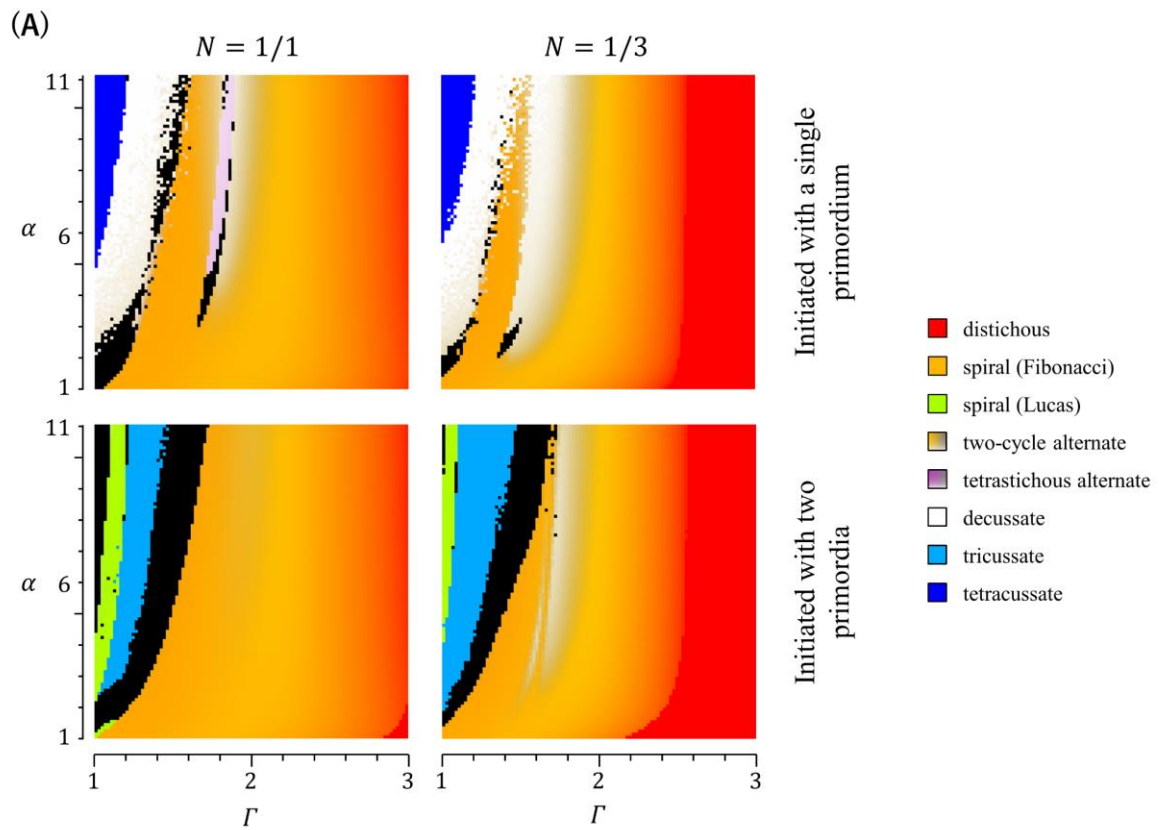
Fig 2-10. Phyllotactic patterns generated in computer simulations using DC2

(A) Computer simulations using DC2 were performed under various settings of parameters α and Γ (101 settings for α and 101 settings for Γ) with $N = 1,\ 1/3,$ or $1/5$, and the resultant patterns are displayed for the cases of $N = 1$ and $1/3$ according to the color legend shown in Fig 2-3. Simulations were started by placing a single primordium or two primordia at a central angle of $120°$ on the SAM periphery. (B) The regular alternate, two-cycle alternate, and tetrastichous four-cycle alternate patterns generated in computer simulations using DC2 in (A), including simulations with $N = 1/5$ as well as $N = 1$ and $1/3$, were plotted using the ratio of absolute values of two successive divergence angles as the abscissa and the ratio of two successive plastochron times as the ordinate. The red dots indicate tetrastichous four-cycle patterns, while the black dots indicate regular alternate and two-cycle patterns. The blue dots show the data of real orixate phyllotaxis observed for winter buds of *O. japonica* (calculated from the data of $P_1{\sim}P_2$ and $P_2{\sim}P_3$ in Fig 2-4D). (C) Magnification of the lower-left corner of (B).
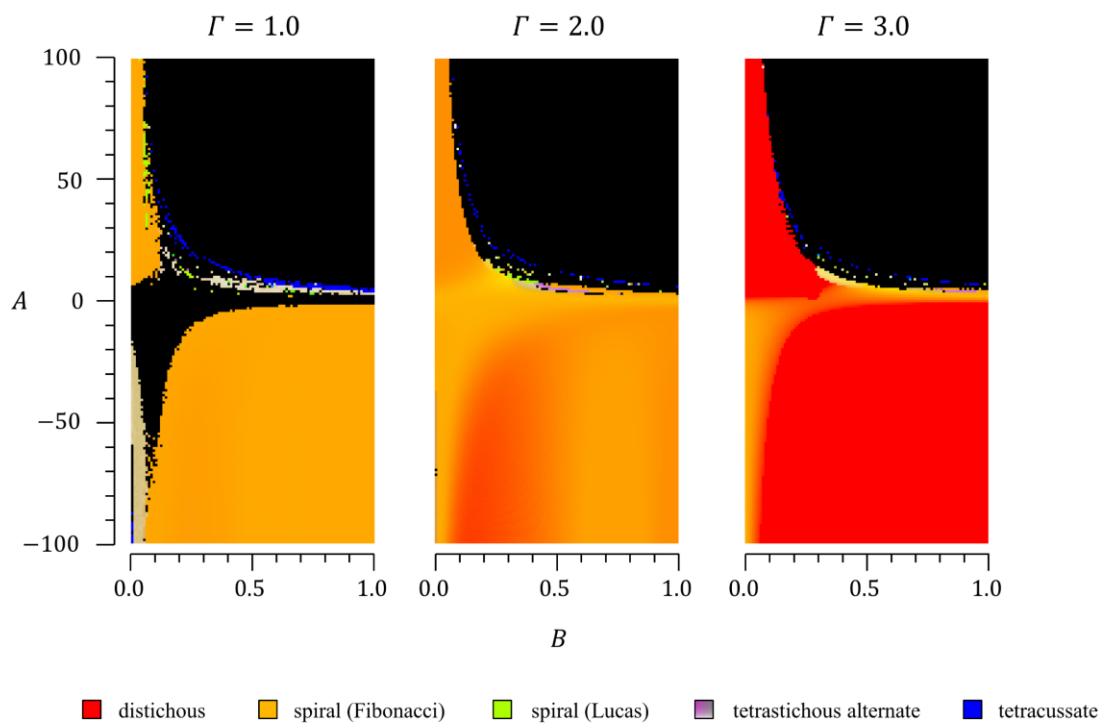
Fig 2-11. Phyllotactic patterns generated in computer simulations using EDC2 with a broad range of settings of *A*

Computer simulations using EDC2 were performed under various parameter settings (201 settings for $-100 \le A \le 100$, 101 settings for B, and 3 settings for Γ), and the patterns obtained are displayed according to the color legend shown in Fig 2-3. Simulations were started by placing a single primordium on the SAM periphery. N was fixed at $1/3$.

(A)

| | distichous | | spiral (Fibonacci) | | spiral (Lucas) | | tetrastichous alternate | | tetracussate |

(B)

47
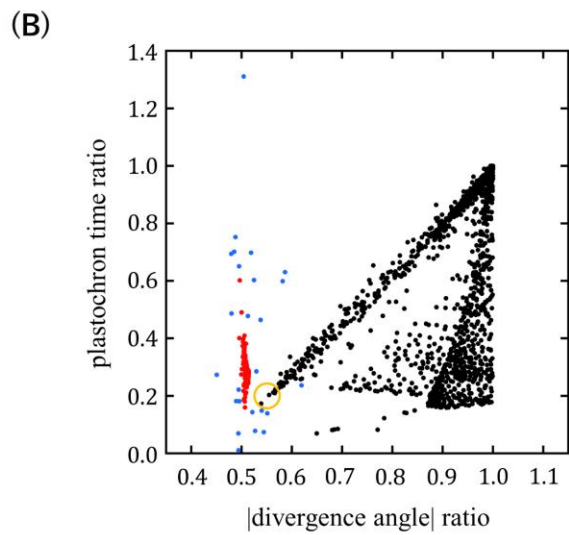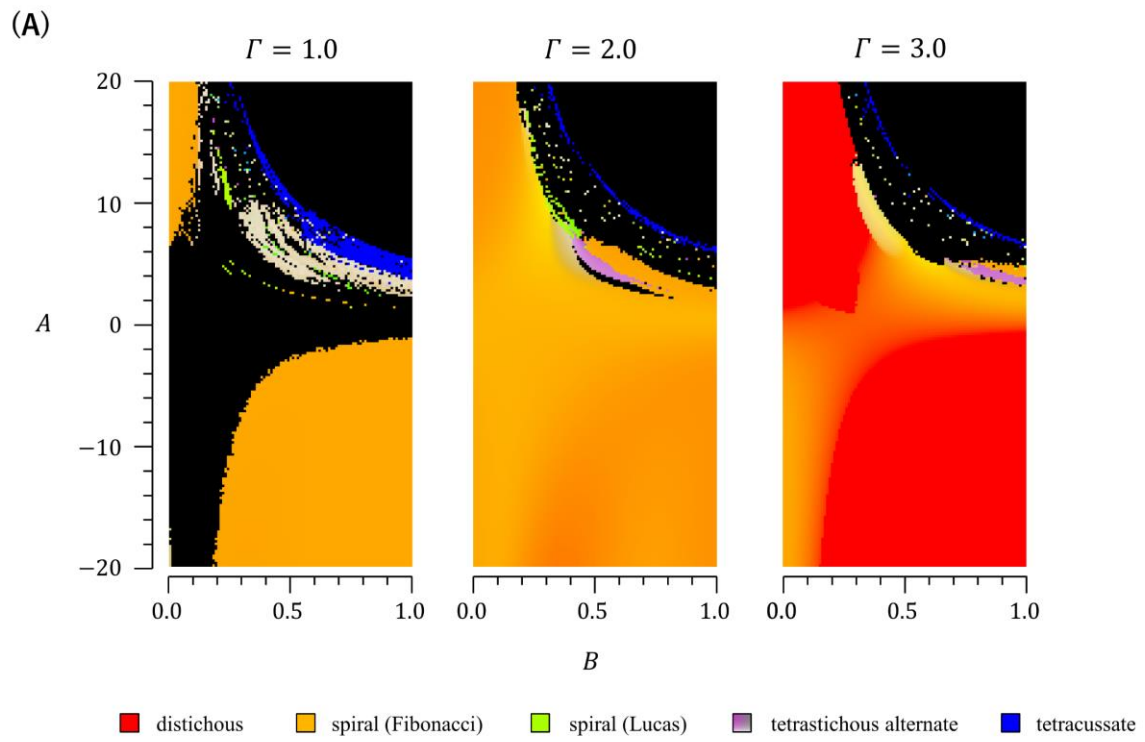
Fig 2-12. Phyllotactic patterns generated in computer simulations using EDC2

(A) Computer simulations using EDC2 were performed under various parameter settings (201 settings for $-20 \leq A \leq 20$, 101 settings for $0 \leq B \leq 1$, and $\Gamma = 1$, 2, or 3) with fixed parameters $\alpha = 1$ and $N = 1/3$, and the patterns obtained are displayed according to the color legend shown in Fig 2-3. Simulations were started by placing a single primordium on the SAM periphery. (B) Computer simulations using EDC2 were performed under various settings of parameters (101 settings for $0 \leq A \leq 20$, 101 settings for $0 \leq B \leq 1$, and $\Gamma = 2$, 2.5, or 3) with fixed parameters $\alpha = 1$ and $N = 1/3$. The graph shows a scatter plot of alternate patterns with a constant divergence angle or a two-cycle change in the divergence angle (black), and tetrastichous alternate patterns with a four-cycle change in the divergence angle (red) generated in the computer simulations. In this graph, each pattern was plotted based on the ratio of absolute values of two successive divergence angles (abscissa) and the ratio of plastochron times (ordinate). The black dots surrounded by an orange circle represent semi-decussate-like patterns that occurred in the vicinities of orixate phyllotaxis in the parameter space, which are indicated by blue asterisks in Fig 2-20. The blue dots indicate the data of real orixate phyllotaxis observed for winter buds of *O. japonica* (calculated from the data of $P_1 \sim P_2$ and $P_2 \sim P_3$ in Fig 2-4D).
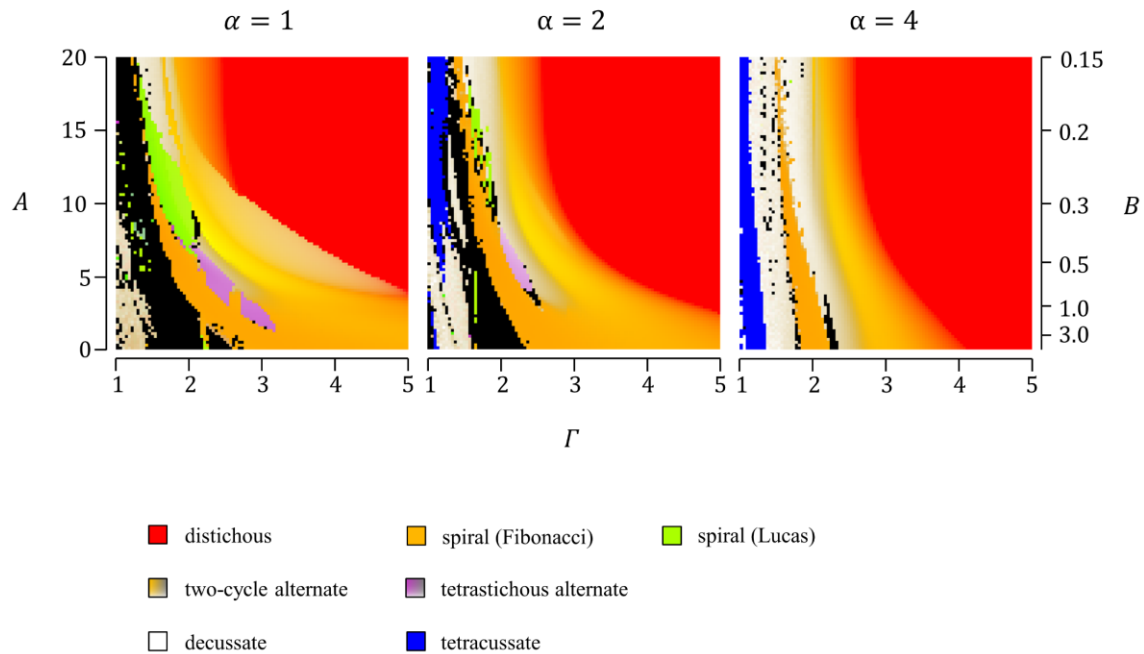
Fig 2-13. Effects of the inhibition range and increase in inhibitory power on phyllotactic patterns in EDC2

Computer simulations were performed using EDC2 with $\alpha = 1,\ 2,$ or 4 under various settings of Γ and A (101×101 conditions), which reflect the maximum inhibition range of a primordium and the primordial age-dependent increase in the inhibitory power, respectively. The initial value of the inhibitory power was fixed to 0.047, i.e., $A \times B$ was fixed at 3. N was fixed at 1/3. The simulation was started by placing a single primordium on the SAM periphery. The patterns obtained are displayed according to the color legend shown in Fig 2-3.

Initiated with a single primordium
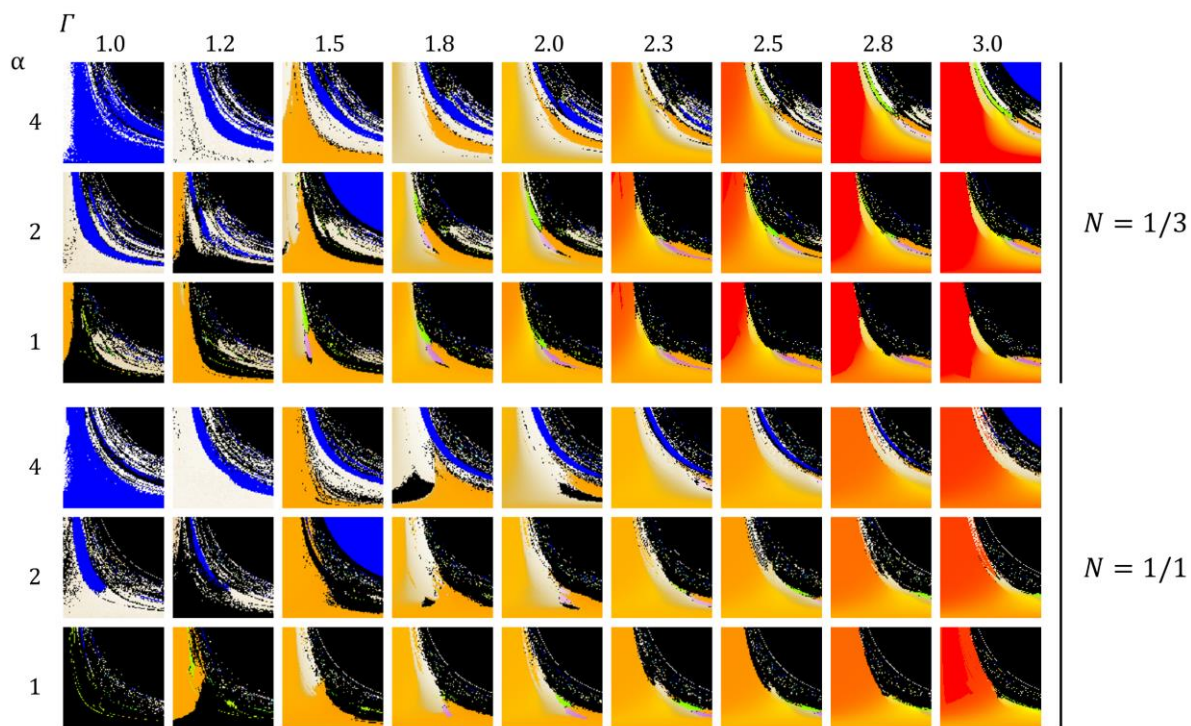
Initiated with two primordia
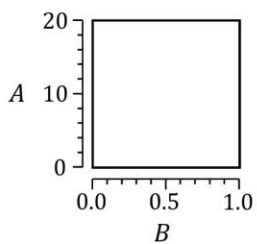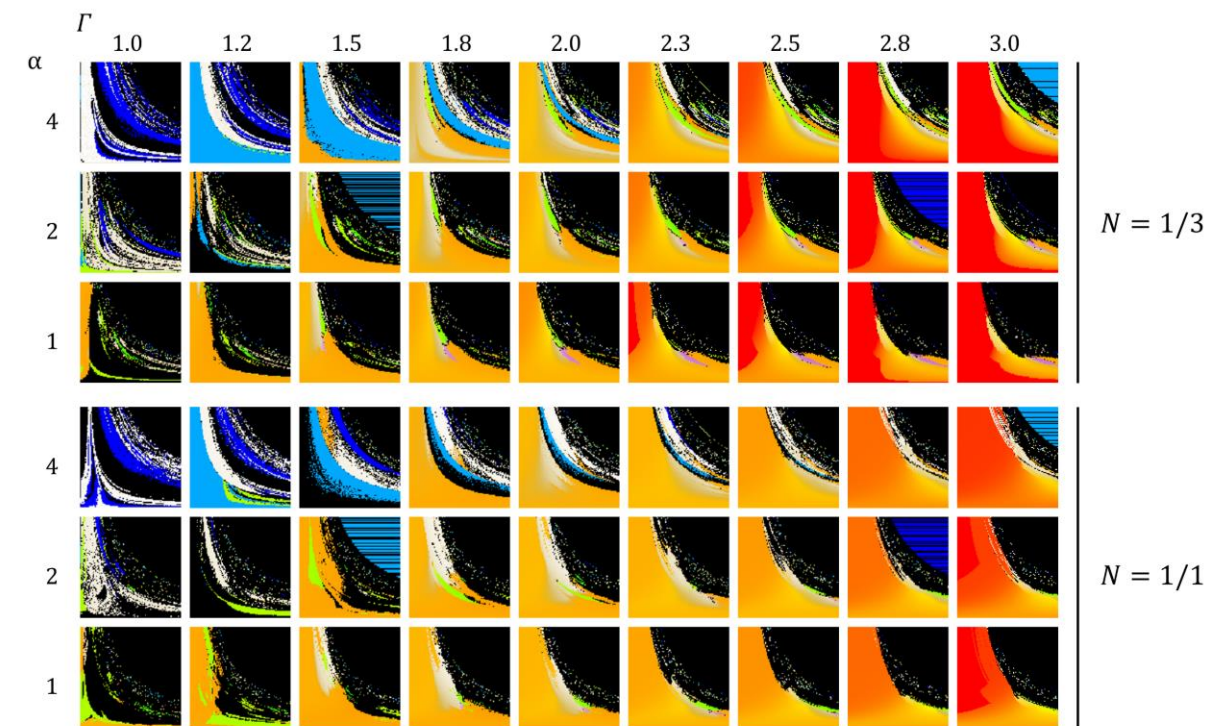
Fig 2-14. Computer simulations using EDC2 over a wide range of combinations of five parameters

A computer simulation was performed using EDC2 under various settings of five parameters, 101 settings for A ($0 \leq A \leq 20$), 101 settings for B ($0 \leq B \leq 1$), 3 settings for α ($\alpha = 1,\ 2,$ or 4), 9 settings for Γ ($1 \leq \Gamma \leq 3$), and 2 settings for N ($N = 1/3$ or 1). The patterns obtained are displayed in the AB space according to the color legend shown in Fig 2-3. Simulations were started by placing a single primordium or two primordia at the central angle of $120°$ on the SAM periphery.

(A)

(B)

(C)
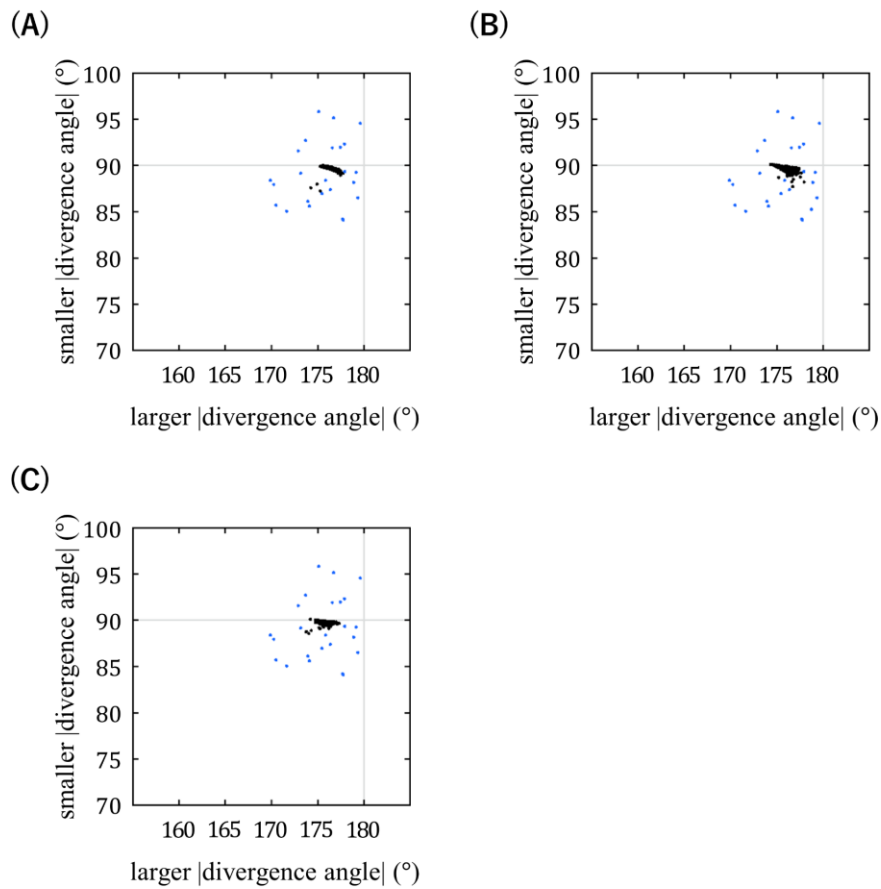
Fig 2-15. Divergence angles of the tetrastichous alternate patterns generated in computer simulations using EDC2

For tetrastichous alternate patterns with a four-cycle change in the divergence angle generated in computer simulations using EDC2 at $\Gamma = 2$ (A), $\Gamma = 2.5$ (B), and $\Gamma = 3$ (C) under the condition of $\alpha = 1$, $N = 1/3$, and $A > 0$, absolute values of divergence angles are plotted using the larger value as the abscissa and the smaller value as the ordinate, such that a pattern with a divergence angle change in the sequence of p, q, $-p$, and $-q$ ($|p| > |q|$) is represented by a dot at the position ($|p|$, $|q|$). The blue dots show the averages determined from the real data of $P_1 \sim P_2$ to $P_6 \sim P_7$ (Fig 2-4D) for each winter bud of *O. japonica*.

(A)

$\Gamma = 2.8$ $N = 1/3$ $\alpha = 1$
$A = 4.8$ $B = 0.72$

(B)
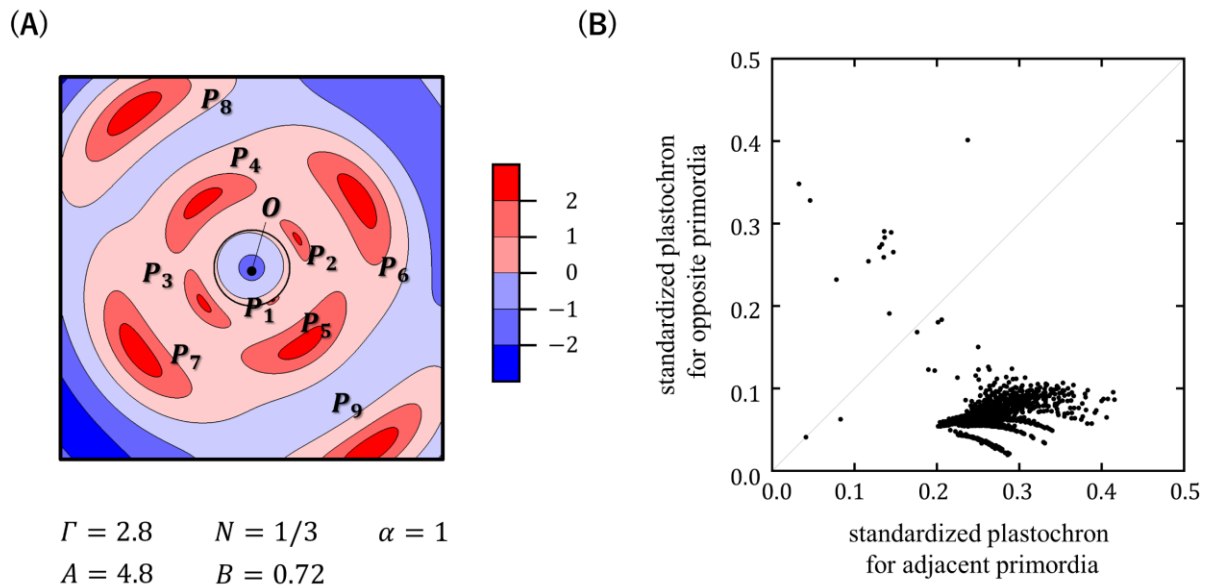
Fig 2-16. Characteristics of orixate patterns generated in computer simulations using EDC2
(A) Contour map of the natural log of the inhibitory field strength I within the shoot apical region that generated orixate phyllotaxis in the computer simulation using EDC2. A value of 0 implies that the inhibitory field strength is equal to the threshold for primordium formation. (B) Relationship between plastochrons and divergence angles in orixate patterns generated in computer simulations using EDC2. For a pair of successive primordia, L_m and L_{m+1}, a standardized plastochron was calculated as $t_{m+1} - t_m = \ln(r_{m+1}/r_m)$. Orixate patterns were plotted based on their two standardized plastochrons: one for the pair of opposite primordia with a divergence angle of approximately 180°, and the other for the pair of adjacent primordia with a divergence angle of approximately $\pm 90^\circ$.

(A)

situation 1   situation 2

(B)

54
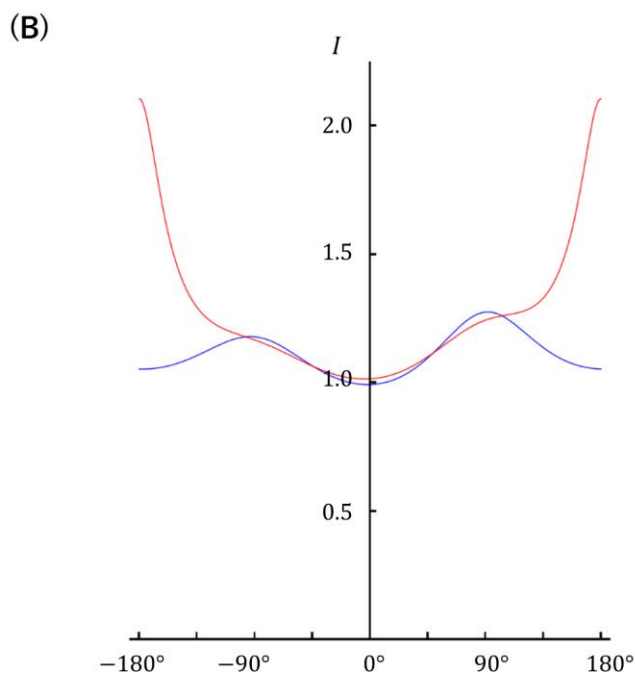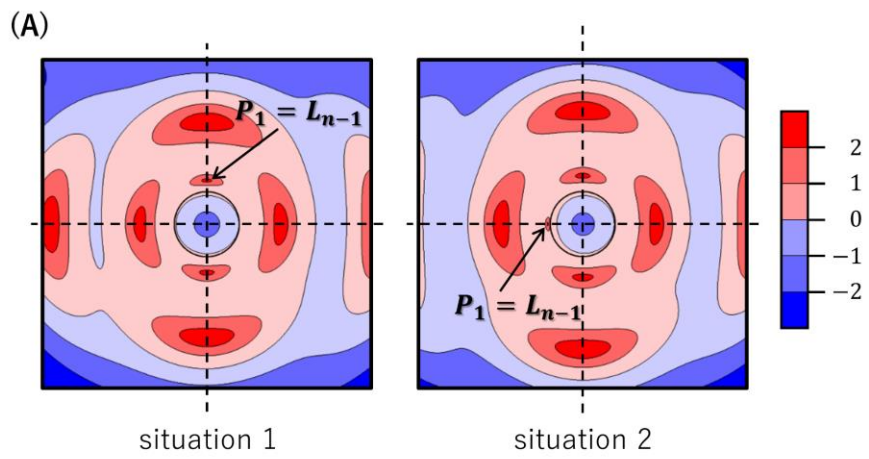
Fig 2-17. Analysis of the stability of the normal orixate phyllotaxis in EDC2

To analyze the stability of the normal orixate phyllotaxis in EDC2, we arranged primordia artificially in the normal orixate pattern with a four-cycle divergence angle change in the sequence of exactly $180°$, $90°$, $-180°$, and $-90°$ and with a standardized plastochron that oscillated between 0.1 and 0.325. We then tested whether the inhibitory field strength could assign the position of a new primordium to maintain the normal orixate pattern in the EDC2 system at the parameter condition ($A = 4.8$, $B = 0.72$, $\Gamma = 2.8$, $N = 1/3$, $\alpha = 1$), with which EDC2 generated a realistic orixate pattern in computer simulation (Fig 2-16A). (A) Contour maps of the natural log of the inhibitory field strength I in the shoot apical region, at which the preceding primordia were artificially arranged in two situations of the normal orixate pattern. (B) The inhibitory field strength on the SAM periphery at the time of formation of the nth primordium L_n was calculated for situation 1 (blue) and situation 2 (red). The inhibitory field strength had a minimum close to the threshold at position $0°$ in both situations, which allows the positioning of a new primordium to maintain the normal orixate pattern.

$\Gamma = 1, \qquad A = 4$

bijugate

tetracussate

bijugate

$\Gamma = 1, \qquad A = 10$

Fibonacci

bijugate

tetracussate

simultaneous formation
of all primordia

$\Gamma = 3, \qquad A = 4$

distichous

two-cycle

(near) Fibonacci

Fibonacci

orixate

$\Gamma = 3, \qquad A = 10$

distichous

simultaneous formation
of all primordia
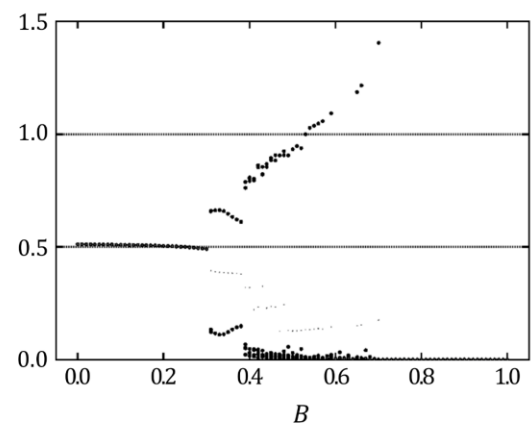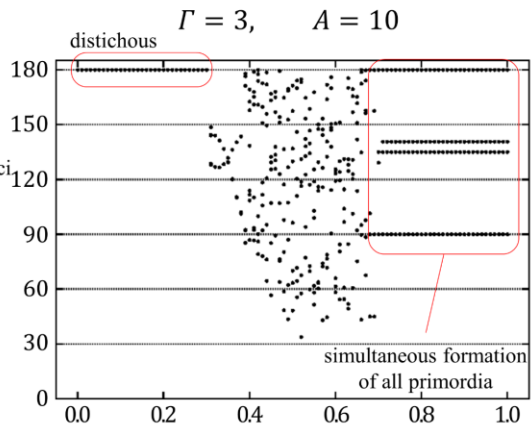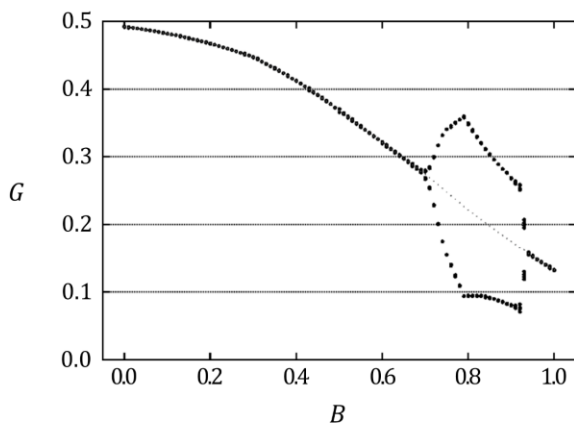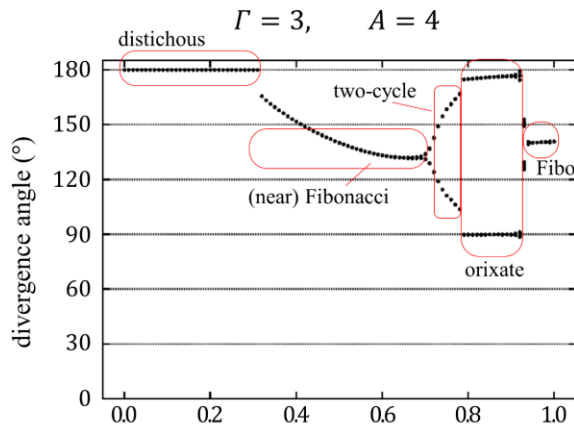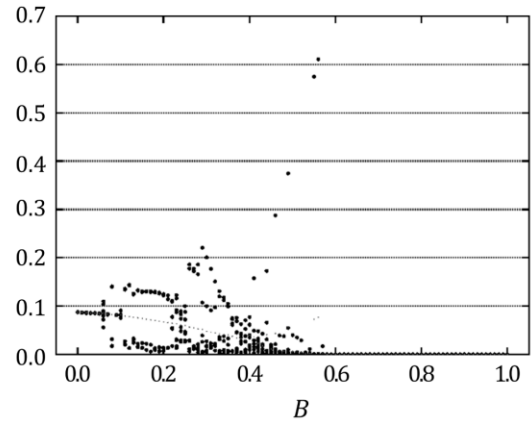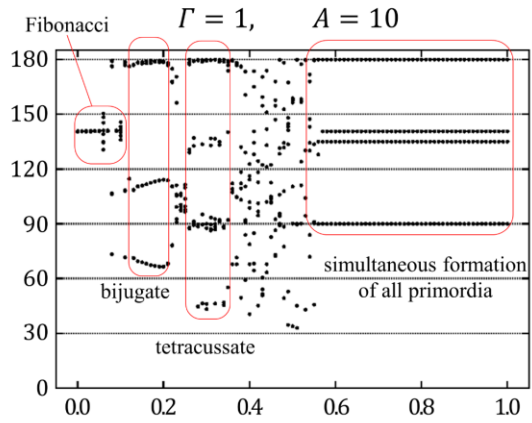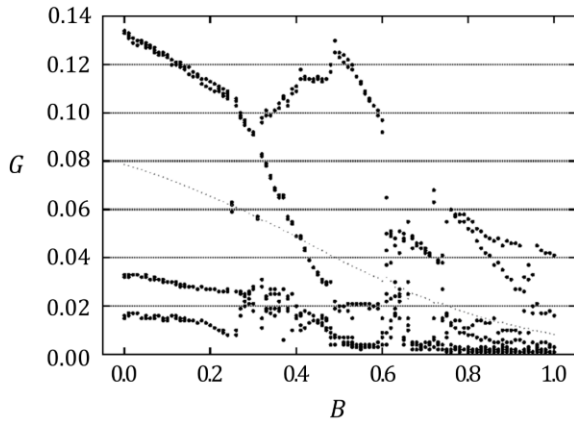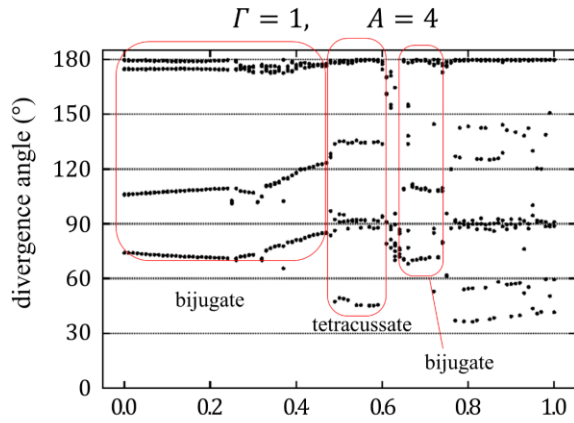
Fig 2-18. Characteristics of phyllotactic patterns generated in computer simulations with EDC2 as influenced by the parameter B

Computer simulations using EDC2 were performed under 101 settings of B ($0 \leq B \leq 1$) at $\Gamma = 1$ or 3, $A = 4$ or 10, and $\alpha = 1$. Divergence angles and the standardized plastochron time G determined from the last nine leaf primordia (L_{92} to L_{100}) are shown for the patterns obtained with various B settings, which represent characteristics of phyllotactic patterns as influenced by the timing of the increase of the inhibitory power.

$\alpha = 1, \quad A = 4$

$\alpha = 1, \quad A = 10$

$\alpha = 4, \quad A = 4$

$\alpha = 4, \quad A = 10$

58
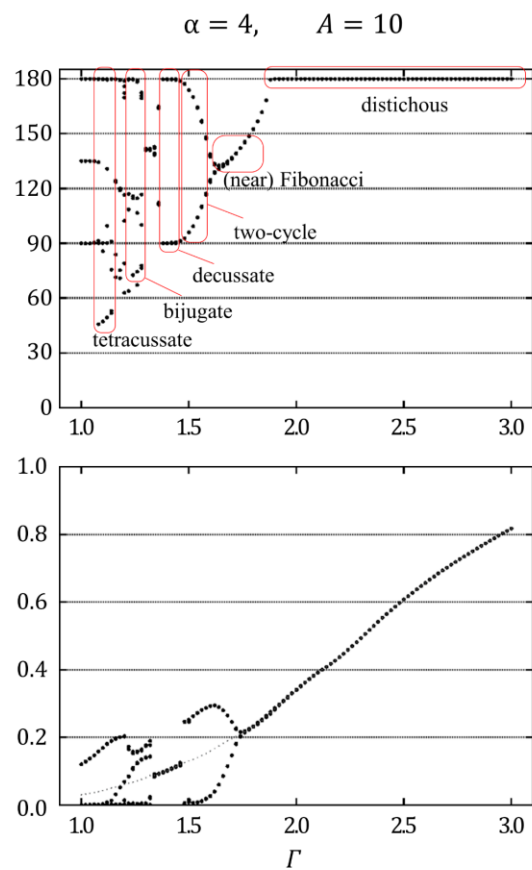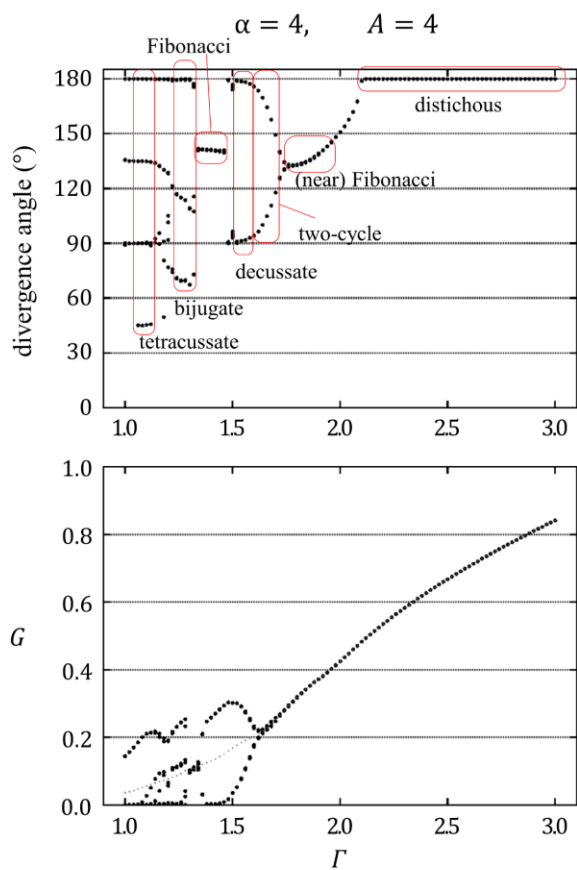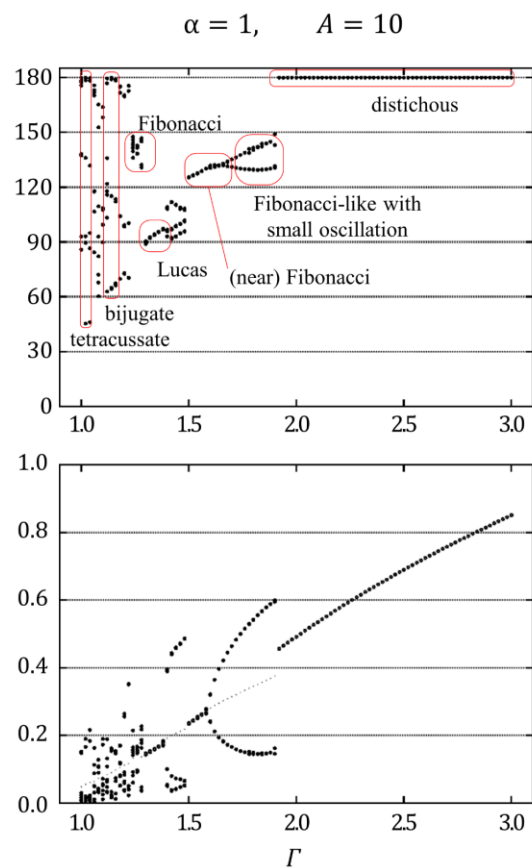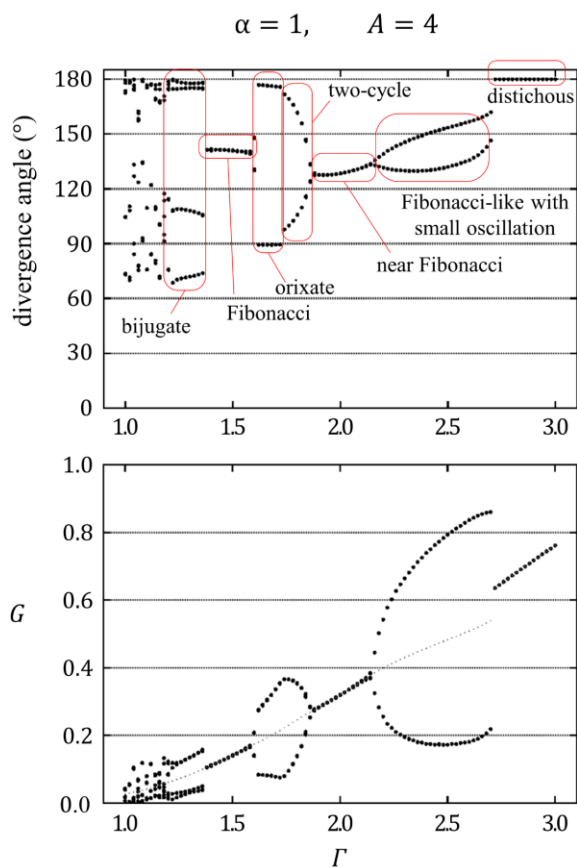
Fig 2-19. Characteristics of phyllotactic patterns generated in computer simulations with EDC2 as influenced by the parameter Γ

Computer simulations using EDC2 were performed under 101 settings of Γ ($1 \leq \Gamma \leq 3$) at $\alpha = 1$ or 4, $A = 4$ or 10, and $A \times B = 3$. Divergence angles and the standardized plastochron time G determined from the last nine leaf primordia (L_{92} to L_{100}) are shown for the patterns obtained with various Γ settings, which represent characteristics of phyllotactic patterns as influenced by the ratio of the inhibition range to the SAM size.

(A) $\alpha = 1, N = 1/3$

$\Gamma = 2.0$

$\Gamma = 2.5$

$\Gamma = 3.0$

(B)

$\Gamma = 2.8 \qquad N = 1/3 \qquad \alpha = 1$
$A = 4.8 \qquad B = 0.68$
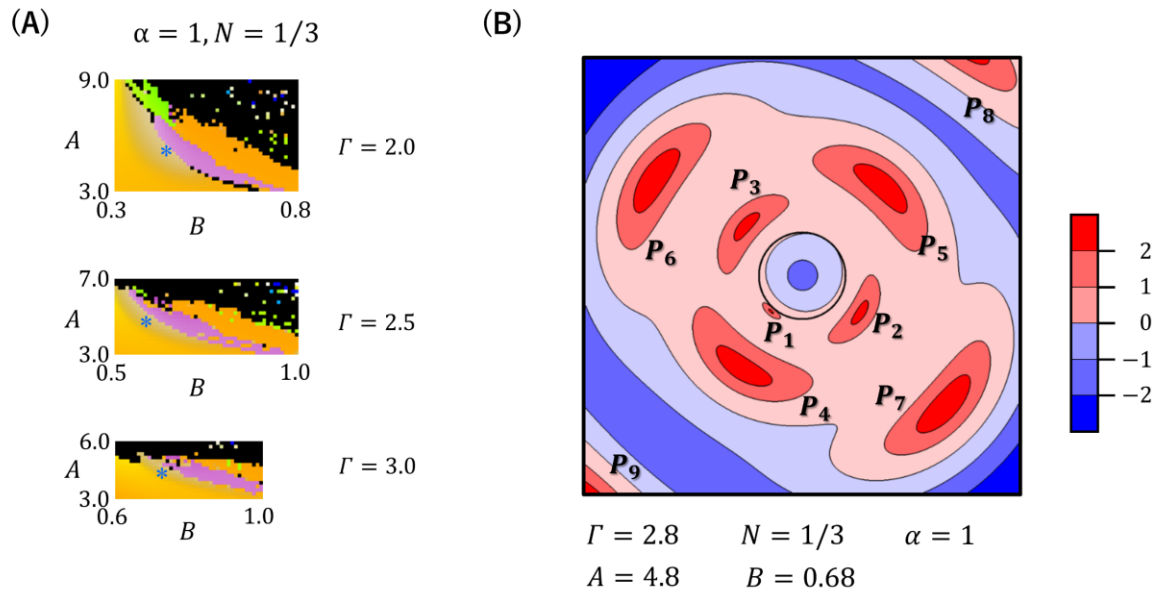
Fig 2-20. Semi-decussate-like patterns generated in computer simulations using EDC2

(A) Computer simulations using EDC2 were performed under various parameter settings (101 settings for $0 \le A \le 20$, 101 settings for $0 \le B \le 1$, and $\Gamma = 2$, 2.5, or 3) with fixed parameters $\alpha = 1$ and $N = 1/3$. The patterns obtained were converted into colors according to the color legend (Fig 2-3), and the areas containing semi-decussate-like patterns (blue asterisks) were cut out from the color diagrams. (B) Contour map of the natural log of the inhibitory field strength I within the shoot apical region generating semi-decussate-like phyllotaxis with divergence angles of 171° and 89° in the computer simulation using EDC2 under the indicated parameter condition.
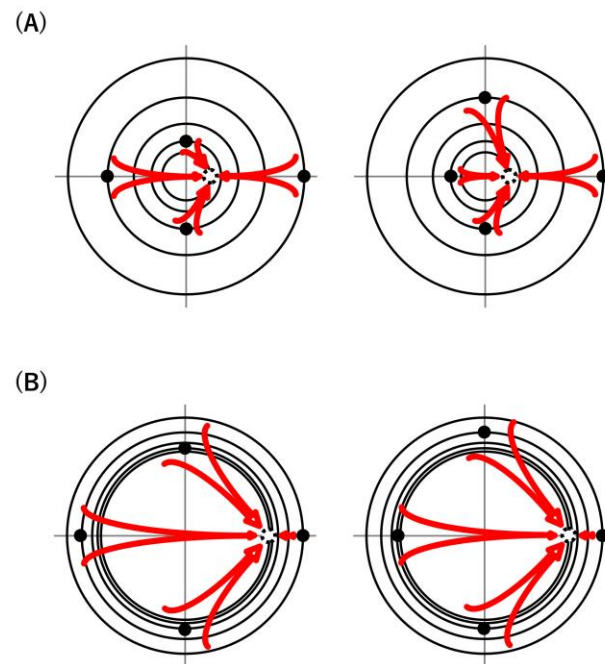
Fig 2-21. Schematic explanation of two conditions that enable orixate phyllotaxis formation
(A) Gradual increase of the inhibitory power with a relatively small size of SAM. (B) Sudden decrease of the inhibitory power with a relatively large size of SAM. EDC1 can establish orixate phyllotaxis under either of these conditions while EDC2 can only under the former condition.

Appendix

Mathematical analysis of the stability of the normal orixate phyllotactic pattern in DC1

In the present section, I considered the stability of normal orixate phyllotaxis, which has ideal periodic repetition of a sequence of divergence angles consisting of exactly $180°$, $90°$, $-180°$, and $-90°$.

Mathematical analysis was performed for the DC1 system, in which the radius of the shoot apical meristem R_0 is 1 and L_i is the ith leaf primordium located at $(r_i \cos\theta_i, r_i \sin\theta_i)$ with $r_i > 1$. The L_i's inhibitory effect $E(x)$ at $(\cos\theta, \sin\theta)$ on the SAM periphery is dependent solely on $d_i(\theta)$, the distance from L_i. When the nth primordium L_n is arising, the inhibitory field strength $I(\theta)$ at the position $(\cos\theta, \sin\theta)$ is calculated by summating the inhibitory effects from all existing primordia, as follows.

$$I(\theta) = \sum_{k=1}^{n-1} E\big(d_k(\theta)\big) = \sum_{j=0}^{3} \sum_{i=1}^{\left|\frac{n-1+j}{4}\right|} E\left(d_{n-4i+j}(\theta)\right) \qquad (2-A1)$$

When the normal pattern of orixate phyllotaxis is stably maintained, the inhibitory field strength should give a minimum at $\theta = \theta_{n-4i}$. Hence, when setting $\theta_{n-4i} = 0$, the following equation should be satisfied:

$$\left.\frac{dI(\theta)}{d\theta}\right|_{\theta=0} = 0 \qquad (2-A2)$$

Because $d_k(\theta) = \sqrt{r_k^2 + 1 - 2r_k \cos(\theta - \theta_k)}$, we obtain:

$$\left.\frac{dd_k(\theta)}{d\theta}\right|_{\theta=0} = \begin{cases} 0 \ (\theta_k = 0, \pi) \\ \mp \dfrac{r_k}{\varrho(r_k)} \left(\theta_k = \pm\dfrac{\pi}{2}\right) \end{cases} \qquad (2-A3)$$

$$d_k(0) = \begin{cases} r_k - 1 \ (\theta_k = 0) \\ r_k + 1 \ (\theta_k = \pi) \\ \varrho(r_k) \left(\theta_k = \pm\dfrac{\pi}{2}\right) \end{cases}, \qquad (2-A4)$$

where $\varrho(r) \equiv \sqrt{r^2 + 1}$.

Thus,

$$\left.\frac{dE\big(d_k(\theta)\big)}{d\theta}\right|_{\theta=0} = \left.\frac{dE(x)}{dx}\right|_{x=d_k(0)} \left.\frac{dd_k(\theta)}{d\theta}\right|_{\theta=0} = \begin{cases} 0 \ (\theta_k = 0, \pi) \\ \mp f(r_k) \left(\theta_k = \pm\dfrac{\pi}{2}\right) \end{cases}, \qquad (2-A5)$$

where $f(r) \equiv \dfrac{r}{\varrho(r)} \left.\dfrac{dE(x)}{dx}\right|_{x=\varrho(r)}$.

Regarding the arrangement of primordia, there are two geometrical situations; in situation 1, the divergence angle between the newly arising primordium, L_n, and the last primordium, L_{n-1}, is $\pm90°$ ($\pm\pi/2$), while it is $180°$ (π) in situation 2 (Fig 2-6A).

(Situation 1)

Situation 1 is represented by setting θ_{n-4i+j} as:

$$\theta_{n-4i+j} = \begin{cases} 0 \ (j=0) \\ \pi \ (j=1) \\ -\dfrac{\pi}{2} \ (j=2) \\ \dfrac{\pi}{2} \ (j=3) \end{cases}. \tag{2-A6}$$

The application of this condition to Eq 2-A5 yields:

$$\left.\frac{dE\left(d_{n-4i+j}(\theta)\right)}{d\theta}\right|_{\theta=0} = \begin{cases} 0 \ (j=0,1) \\ f\left(r_{n-4i+j}\right) \ (j=2) \\ -f\left(r_{n-4i+j}\right) \ (j=3) \end{cases}. \tag{2-A7}$$

Hence,

$$\left.\frac{dI(\theta)}{d\theta}\right|_{\theta=0} = \sum_{j=0}^{3} \sum_{i=1}^{\left\lfloor\frac{n-1+j}{4}\right\rfloor} \left.\frac{dE\left(d_{n-4i+j}(\theta)\right)}{d\theta}\right|_{\theta=0}$$

$$= \sum_{i=1}^{\left\lfloor\frac{n+1}{4}\right\rfloor} f(r_{n-4i+2}) - \sum_{i=1}^{\left\lfloor\frac{n+2}{4}\right\rfloor} f(r_{n-4i+3}). \tag{2-A8}$$

Because $E(x)$ is a monotonically decreasing function, $f(r)$ is always negative:

$$\left.\frac{dI(\theta)}{d\theta}\right|_{\theta=0} \geq \sum_{i=1}^{\left\lfloor\frac{n+1}{4}\right\rfloor} \{f(r_{n-4i+2}) - f(r_{n-4i+3})\}. \tag{2-A9}$$

(Situation 2)

Situation 2 is represented by setting θ_{n-4i+j} as:

$$\theta_{n-4i+j} = \begin{cases} 0 \ (j=0) \\ -\dfrac{\pi}{2} \ (j=1) \\ \dfrac{\pi}{2} \ (j=2) \\ \pi \ (j=3) \end{cases}. \tag{2-A10}$$

The θ-derivative of $I(\theta)$ can be calculated as in the case described for situation 1:

$$\left.\frac{dI(\theta)}{d\theta}\right|_{\theta=0} = \sum_{i=1}^{\left\lfloor\frac{n}{4}\right\rfloor} f(r_{n-4i+1}) - \sum_{i=1}^{\left\lfloor\frac{n+1}{4}\right\rfloor} f(r_{n-4i+2})$$

$$\geq \sum_{i=1}^{\left\lfloor\frac{n}{4}\right\rfloor} \{f(r_{n-4i+1}) - f(r_{n-4i+2})\}. \tag{2-A11}$$

According to the distance dependency of the inhibitory effect assumed in DC1, $E(\varrho) = k\varrho^{-\eta}$. Using this assumption and noting that $\eta > 0$ and $r > 1$, we obtain:

$$\frac{df(r)}{dr} = \frac{d}{dr}\left(\frac{r}{\varrho}\frac{d}{d\varrho}k\varrho^{-\eta}\right) = k\eta\varrho^{-\eta-4}\{(\eta+1)r^2 - 1\} > 0. \qquad (2-A12)$$

As $f(r)$ increases monotonically with r, $f(r_{n-4i+1}) > f(r_{n-4i+2}) > f(r_{n-4i+3})$, and then $\left.\frac{dI(\theta)}{d\theta}\right|_{\theta=0} >$

0 in both situations. This indicates that the total inhibitory field strength cannot satisfy Eq 2-A2, which demonstrates that normal orixate phyllotaxis cannot be established in DC1.

Chapter III
　本章については、5 年以内に雑誌等で刊行予定のため非公開。

Chapter IV
　本章については、5 年以内に雑誌等で刊行予定のため非公開。

Chapter V

Concluding remarks

In the present studies, I aimed at exploring the fundamental mechanism controlling the positions of leaf primordia that can account for the comprehensive generation of all phyllotactic patterns in agreement with their natural occurrence. For this purpose, I performed extensive analyses, particularly by mathematical modeling, on two uncommon types of phyllotaxis that had been unaddressed in the previous mechanistic models, orixate phyllotaxis and costoid phyllotaxis.

I first focused on orixate phyllotaxis, which is characterized by the four-cycle periodic repetition of the sequences of divergence angle; 180°, 90°, 180°, and 270° (Maekawa, 1948). Orixate phyllotaxis is found in several distant taxa (Maekawa, 1948; Snow, 1958), implying that it does not require a specialized mechanism but can be generated by a universal mechanism. The concept that new leaf primordia emerge in the largest gap between existing primordia, called Hofmeister's axiom, was empirically derived from early observations (Hofmeister, 1868) and is now believed to underlie the universal mechanism of phyllotactic pattern formation. DC models (alternate-specific form, DC1; more generalized form, DC2) are representatives of the abstract mathematical models of the inhibitory-field type conforming to Hofmeister's axiom and serving as a theoretical framework of phyllotactic patterning, in which each leaf primordium is assumed to emit a constant level of power inhibiting vicinal primordium formation (Douady and Couder, 1996a; 1996b). I tested, by exhaustive computer simulations, the ability of these models to produce orixate phyllotaxis but the results were negative for either DC1 or DC2. Then I expanded them by introducing primordial age-dependent changes in the inhibitory power and succeeded in generating orixate phyllotaxis by simulations with the expanded version of DC2 (EDC2) when the inhibitory power was set to increase late and slowly. Moreover, EDC2 was found to give a better explanation to the frequencies of various phyllotactic patterns in nature, including the overwhelming dominance of Fibonacci spiral among spirals, than DC2 and the other previous models. From these findings, I concluded that the age-dependent increase of the inhibitory power is necessary to generate orixate phyllotaxis and is generally involved in the mechanism of leaf primordium positioning and phyllotactic patterning.

Next, I considered the possible molecular basis for the hypothetical age-dependent increase of inhibitory power using theoretical approach. Recent findings from molecular biological studies on the roles of auxin and its polar transport in leaf primordium formation have been integrated into the auxin-transport-based models, which assume that auxin convergence spontaneously arisen through the positive feedback loop between auxin gradient and polar transport triggers leaf primordium initiation and were demonstrated to be able to produce several major types of phyllotaxis (Jönsson et al., 2006; Smith et al., 2006). As in these models depletion of auxin by drainage into the auxin convergence creates an inhibitory field (Mirabet et al., 2012), the increase of the inhibitory power in EDC models was expected to reflect the expansion of the range within which the auxin convergence drains auxin. However, computer simulation analysis with the simplest auxin-transport-based model (Jönsson et al., 2006) of which auxin dynamics is uniform and constant showed that the expansion of the auxin drainage area does occur but that it is too fast to satisfy the requirements for orixate phyllotaxis. Then, I modified the auxin-transport-based model by adding the assumption that the auxin drainage area around the auxin convergence expands not only in dependence on the basic auxin dynamics but also in association with primordial growth. Computer simulations using this model generated orixate-phyllotaxis-like

patterns at several conditions where the auxin drainage area expanded late and slowly. These patterns, however, were always unstable, which implicated some additional mechanisms in the stabilization of orixate phyllotaxis.

Finally, I focused on costoid phyllotaxis, which is unique to Costaceae, Zingiberales and is distinguished by its steep spiral with a very small divergence angle from common spiral phyllotaxis (Nakai, 1941). Costoid phyllotaxis seems incompatible with the Hofmeister's axiom (Hofmeister, 1868) and therefore has been recognized as a "genuine puzzle" in the study on phyllotaxis (Jean, 1994). In an attempt to generate costoid phyllotaxis in silico, by adding a hypothetical effect of the preceding primordium that induces primordium formation in its vicinity into EDC2, I constructed a new mathematical model assuming both inductive and inhibitory fields (YS model for the Japanese words "Yūdou" for induction and "Sogai" for inhibition). Computer simulations with YS model gave the same results as simulations with EDC2 over a wide range of conditions and failed to form primordia at the other wide range of conditions. Within the narrow range between these two conditions, where increases in the inductive and inhibitory effects were competed in a balanced relation, costoid phyllotaxis was obtained as a stable pattern. Interestingly, one-sided distichous phyllotaxis also occurred in this range at slightly different parameter settings. Considering that one-sided distichous phyllotaxis as well as costoid phyllotaxis are characteristic to plants of Zingiberales, generation of these phyllotactic patterns at similar conditions in YS model is very suggestive for the validity of this model. In seedlings of *C. megalobractea*, the divergence angle was found to be smaller in younger pairs of leaves. Such change in the divergence angle was reproduced in YS model when assuming a gradual increase of the SAM size during seedling growth, which is common among plants. This result provides another evidence for YS model. These findings collectively suggest involvement of some inductive effect from the preceding primordium in leaf positioning for the first time and show that the competitive expansion of the induction and inhibition ranges can account for the generation of costoid phyllotaxis.

My studies on uncommon phyllotaxes revealed novel aspects of the general mechanism of leaf positioning and phyllotactic pattern formation, and I constructed new mathematical models, EDCs and YS, by incorporating these aspects. All these models are expected to be very useful for analyzing the natural phyllotactic variety. YS model is most comprehensive among them, but the inductive power hypothesized in this model is influential only in the generation of costoid or one-sided distichous phyllotaxis in Zingiberales. As EDC2 is substantially sufficient for producing almost all types of phyllotaxis other than these two phyllotaxes, I here propose EDC2 as the most appropriate abstract model for the practical simulation of phyllotactic pattern formation.

After these studies, there still remain several questions for the fundamental mechanisms of phyllotactic patterning and some questions have newly arisen. The most important questions are what molecular processes are responsible for the inhibitory and inductive interactions between leaf primordia and how they are regulated with the primordial age. Although the polar transport and concentration gradient of auxin have been linked to the inhibitory interaction, details of their regulatory system including its change during leaf primordium development has not yet been elucidated. In addition to the auxin-transport-based mechanism, some mechanisms were suggested to participate in the stabilization of orixate phyllotaxis, but it is totally unknown

what they are. The inductive interaction in YS model is just hypothetical and I have no experimental clues for it. Further studies on uncommon phyllotaxes by combination of mathematical model analysis and molecular biological analysis would open a way to answer these questions.

Phyllotaxis has long attracted researchers because of their interest not only in its pattern formation process but also in its adaptive evolution. To give an example, Fibonacci spiral is supposed to have advantage in light capture and be adaptive at least in some environmental circumstances (Niklas, 1988; Pearcy and Yang, 1998; King et al., 2004; Strauss et al., 2019). However, it is not clear whether such putative advantage have really driven the phyllotactic pattern evolution largely due to the lack of the developmental viewpoints. For solving this great problem, it seems necessary to consider any ecological advantages or disadvantages of various types of phyllotaxis on possible paths of evolution of phyllotaxis under the developmental constraints. The parameter spaces of my models EDC2 and YS may provide platforms to deal with the developmentally constrained evolution paths of phyllotactic patterns and contribute to understanding of both the proximate and ultimate causes of phyllotactic patterns.

References

Adler I. (1974). A model of compact pressure in phyllotaxis. J Theor Biol. 45: 1–79.

Bayer EM, Smith RS, Mandel T, Nakayama N, Sauer M, Prusinkiewicz, P, Kuhlemeier C. (2009). Integration of transport-based modelsfor phyllotaxis and midvein formation. Genes Dev. 23: 373–384.

Benková E, Michniewicz M, Sauer M, Teichmann T, Seifertová D, Jürgens G, Friml J. (2003), Local, efflux-dependent auxin gradient as a common module for plant organ formation. Cell. 115: 591–602.

Berger A. (1908). Liliaceae-Asphodeloideae-Aloinae. In: Engler A, editor. Das Pflanzenreich. Leipzig: Verlag von Wilhelm Engelmann; 33 Heft; IV, 38, III, II.

Bernasconi GP. (1994). Reaction-diffusion model for phyllotaxis. Physica D. 70: 90–99.

Besnard F, Refahi Y, Morin V, Marteaux B, Brunoud G, Chambrier P, Rozier F, Mirabet V, Legrand J, Lainé S, Thévenon E, Farcot E, Cellier C, Das P, Bishopp A, Dumas R, Parcy F, Helariutta Y, Boudaoud A, Godin C, Traas J, Guédon Y, Vernoux T. (2014). Cytokinin signalling inhibitory fields provide robustness to phyllotaxis. Nature. 505: 417-421.

Cheng Y, Dai X, Zhao Y. (2007). Auxin synthesized by the YUCCA flavin monooxygenases is essential for embryogenesis and leaf formation in *Arabidopsis*. Plant Cell. 19: 2430-2439.

Cole TCH, Hilger HH, Stevens P. (2019). Angiosperm phylogeny poster – Flowering plant systematics, 2019; 2019/2 with links to APweb.

Dan H, Imaseki H, Wasteneys GO, Kazama H. (2003). Ethylene stimulates endoreduplication but inhibits cytokinesis in cucumber hypocotyl epidermis. Plant Phys. 133: 1726-1731.

Douady S, Couder Y. (1992). Phyllotaxis as a physical self-organized growth process. Phys Rev Lett. 68: 2098–2101.

Douady S, Couder Y. (1996a). Phyllotaxis as a dynamical self organizing process Part I: The spiral modes resulting from time-periodic iterations. J Theor Biol. 178: 255–274.

Douady S, Couder Y. (1996b). Phyllotaxis as a dynamical self organizing process Part II: The spontaneous formation of a periodicity and the coexistence of spiral and whorled patterns. J Theor Biol. 178: 275–294.

Douady S, Couder Y. (1996c). Phyllotaxis as a dynamical self organizing process Part III: The simulation of the transient regimes of ontogeny. J Theor Biol. 178: 295–312.

Farhadifar R, Roper JC, Aigouy B, Eaton S, Julicher F. (2007). The influence of cell mechanics, cell-cell interactions, and proliferation on epithelial packing. Curr Biol. 17: 2095–2104.

Fletcher AG, Osterfield M, Baker RE, Shvartsman SY. (2014). Vertex models of epithelial morphogenesis. Biophys J. 106: 2291–2304.

Fozard JA, Lucas M, King JR, Jensen OE. (2013). Vertex element models for anisotropic growth of

elongated plant organs. Frontiers Plant Sci. 4: 233.

Fujita H, Kawaguchi M. (2013). Pattern formation by two-layer Turing system with complementary synthesis. J Theor Biol. 322: 33–45.

Fujita H, Kawaguchi M. (2018). Spatial regularity control of phyllotaxis pattern generated by the mutual interaction between auxin and PIN1. PLOS Comp Biol. 14: e1006065.

Galvan-Ampudia CS, Cerutti G, Legrand J, Azais R, Brunoud G, Moussu S, Wenzl C, Lohmann JU, Godin C, Vernoux T. (2019). From spatio-temporal morphogenetic gradients to rhythmic patterning at the shoot apex. bioRxiv. 469718.

Goebel K. (1904). Die Entfaltungsbewegungen der Pflanzen und deren teleologische. Deutung. G. Fischer, Jena.

Goebel K. (1908). Organographie der Pflanzen. Vol. 1. G. Fischer, Jena.

Goldsmith MHM. (1966). Maintenance of polarity of auxin movement by basipetal transport. Plant Phys.41: 749-754.

Goldsmith MHM, Goldsmith TH, Martin MH. (1981). Mathematical analysis of the chemosmotic polar diffusion of auxin through plant tissues. PNAS. 78: 976-980.

Green PB. (1992). Pattern formation in shoots: a likely role for minimal energy configurations of the tunica. Int J Plant Sci. 153: S59–S75.

Green PB, Steele C, Rennich S. (1996). Phyllotactic patterns: A biophysical mechanism for their origin. Ann Bot. 77: 515–518.

Heisler MG, Bryne ME. (2020). Progress in understanding the role of auxin in lateral organ development in plants. Curr Opin Plant Biol. 53: 73-79.

Hirmer M. (1922). Zur Losung des Problems der Blattstellungen. G. Fisher, Jena.

Hofmeister W. (1868). Allgemeine Morphologie des Gewachse. Engelmann, Leipzig.

Hotton S, Johnson V, Wilbarger J, Zwieniecki K, Atela P, Golé C, Dumais J. (2006). The possible and the actual in phyllotaxis: Bridging the gap between empirical observations and iterative models. J Plant Growth Regul. 25: 313–323.

Jean RV. (1988). Phyllotactic pattern generation: a conceptual model. Ann Bot. 61: 293-303.

Jean RV. (1994). Phyllotaxis: A systemic study in plant morphogenesis. Cambridge: Cambridge University Press.

Jha RM, Bokhari SA, Wiesbeck W. (1993). A novel ray tracing on general paraboloids of revolution for UTD applications. IEEE Trans ant Prop. 41: 934-939.

Jönsson H, Heisler M, Shapiro B, Meyerowitz E, Mjolsness E. (2006). An auxin-driven polarized transport model for phyllotaxis. PNAS. 103: 1633–1638.

King S, Beck F, Lüttge U. (2004). On the mystery of the golden angle in phyllotaxis. Plant Cell Env. 27: 685-695.

Kirchoff BK. (1986). Inflorescence structure and development in the Zingiberales: *Thalia geniculata* (Marantaceae). Can J Bot. 64: 859-864.

Kirchoff BK and Rutishauser R. (1990). The phyllotaxy of *Costus* (Costaceae). Bot Gaz. 151: 88-105.

Kitazawa MS, Fujimoto K. (2015). A dynamical phyllotaxis model to determine floral organ number. PLOS Comput Biol. 2015; 11: e1004145.

Kitazawa MS, Fujimoto K. (2018). Spiral phyllotaxis underlies constrained variation in *Anemone* (Ranunculaceae) tepal arrangement. J Plant Res. 131: 459–468.

Kramer EM, Rutschow HL, Mabie SS. (2011). AuxV: a database of auxin transport velocities. Trends Plant Sci. 16: 461-463.

Levitov LS. (1991a). Phyllotaxis of flux lattices in layered superconductors. Phys Rev Lett. 66: 224–227.

Levitov LS. (1991b). Energetic approach to phyllotaxis. Europhys Lett. 14: 533-539.

Levitov LS. (1991c). Fibonacci numbers in botany and physics: Phyllotaxis. JETP Lett. 54: 546–550.

Maekawa F. (1948). Folia orixata, a new type of phyllotaxis and its significance to phyllotaxis evolution. Bot Mag Tokyo. 61: 7–10.

Martinez CC, Koenig D, Chitwood DH, Sinha NR. (2016). A sister of PIN1 gene in tomato (*Solanum lycopersicum*) defines leaf and flower organ initiation patterns by maintaining epidermal auxin flux. Dev Biol. 419: 85–98.

Medford JI, Behringer FJ, Callos JD, Feldmann KA. (1992). Normal and abnormal development in the Arabidopsis vegetative shoot apex. Plant Cell. 4: 631-643.

Meinhardt H. (1982). Models for biological pattern formation. London: Academic Press.

Mirabet V, Besnard F, Vernoux T, Boudaoud A. (2012). Noise and robustness in phyllotaxis. PLOS Comput Biol. 8: e1002389.

Mitchson G. (1977). Phyllotaxis and the Fibonacci series. Science. 196: 270–275.

Mitchson G. (1980). The dynamics of auxin transport. Phil Trans Roy B. 209: 489-511.

Nakai T. (1941). Notulæ ad plantas Asiæ orientalis (XVI). J Japanese Bot. 17: 189-210.

Newell AC, Shipman PD, Sun Z. (2008). Phyllotaxis: Cooperation and competition between mechanical and biochemical processes. J Theor Biol. 251: 421–439.

Niklas KJ. (1988). The role of phyllotactic pattern as a "developmental constraint" on the interception of light by leaf surfaces. Evolution. 42: 1-16.

Okabe T. (2016). The riddle of phyllotaxis exquisite control of divergence angle. Acta Soc Bot Pol. 85: 3527.

Pearcy RW, Yang W. (1998). The functional morphology of light capture and carbon gain in the Redwood forest understorey plant *Adenocaulon bicolor* Hook. Func Ecol. 12: 543-552.

Refahi Y, Brunoud G, Farcot E, Jean-Marie A, Pulkkinen M, Vernoux T, Godin, C. (2016). A stochastic multicellular model identifies biological watermarks from disorders in self-organized patterns of phyllotaxis. eLife. 5: e14093.

Reinhardt D, Mandel T, Kuhlemeier C. (2000). Auxin regulates the initiation and radial position of plant lateral organs. Plant Cell. 12: 507–518.

Reinhardt D, Pesce E, Stieger P, Mandel T, Baltensperger K, Bennett M, Traas J, Friml J, Kuhlemeier C. (2003). Regulation of phyllotaxis by polar auxin transport. Nature. 426: 255–260.

Richards FJ. (1951). Phyllotaxis: its quantitative expression and relation to growth in the apex. Phil Trans R Soc London B. 225: 509–564.

Roberts DW. (1977). A contact pressure model for semi-decussate and related phyllotaxis. J Theor Biol. 68: 583–597.

Rueda-Contreras MD, Romero-Arias JR, Aragón JL, Barrio RA. (2018). Curvature-driven spatial patterns in growing 3D domains: A mechanochemical model for phyllotaxis. PLoS ONE. 13: e0201746.

Rutishauser R. (1998). Chapter 8. Plastochron ratio and leaf arc as parameters of a quantitative phyllotaxis analysis in vascular plants. In: Jean RV and Barabé D, editor. Symmetry in Plants. World Scientific. 171-212.

Schüepp O. (1928). Untersuchungen und Konstruktionen zur Theorie der einfachen Spiralstellung. Jahrb Wiss Bot. 5:867-886.

Schumann K. (1892). Morphologische Studien. Engelmann, Leipzig.

Schumann K. (1902). Marantaceae. In: Engler A, editor. Das Pflanzenreich. Leipzig: Verlag von Wilhelm Engelmann; 11 Heft; IV, 48.

Schumann K. (1904). Zingiberaceae. In: Engler A, editor. Das Pflanzenreich. Leipzig: Verlag von Wilhelm Engelmann; 20 Heft; IV, 46.

Shinkle JR, Kadakia R, Jones AM. (1998). Dim-red-light-induced increase in polar auxin transport in cucumber seedlings: I. Development of altered capacity, velocity, and response to inhibitors. Plant Phys. 116: 1505-1513.

Shipman PD, Newell AC. (2004). Phyllotactic patterns on plants. Phys Rev Lett. 92: 168102.

Smith BW. (1941). The phyllotaxis of *Costus* from the standpoint of development. Proc Leeds Philos Lit Soc. (Sci Sec.) 4: 42-63.

Smith RS, Guyomarc'h S, Mandel T, Reinhardt D, Kuhlemeier C, Prusinkiewicz, P. (2006a). A plausible model of phyllotaxis. PNAS. 103: 1301–1306.

Smith RS, Khulemeier C, Prusinkiewicz P. (2006b) Inhibition fields for phyllotactic pattern formation: A

simulation study. Can J Bot. 84: 1635–1639.

Snow M, Snow R. (1962). A theory of the regulation of phyllotaxis based on *Lupinus albus*. Phil Trans Roy B. 244: 483–513.

Snow R. (1952). On the shoot apex and phyllotaxis of *Costus*. New Phytol. 51: 359–363.

Snow R. (1958). Phyllotaxis of *Kniphofia* and *Lilium candium*. New Phytol. 57: 160–167.

Strauss S, Lempe J, Prusinkiewicz P, Tsiantis M, Smith RS. (2019). Phyllotaxis: is the golden angle optimal for light capture? New Phytol. 225: 499-510.

Thompson AM, Crants J, Schnable PS, Yu J, Timmermans MCP, Springer NM, Scanlon MJ, Muehlbauer GJ. (2014). Genetic control of maize shoot apical meristem architecture. G3. 4: 1327-1337.

Trichas G, Smith AM, White N, Wilkins V, Watanabe T, Moore A, Joyce B, Sugnaseelan J, Rodriguez TA, Kay D, Baker RE, Maini PK, Srinivas S. (2012). Multi-Cellular Rosettes in the Mouse Visceral Endoderm Facilitate the Ordered Migration of Anterior Visceral Endoderm Cells. PLOS Biol. 10: e1001256.

Troll W. (1937). Vergleichende Morphologie der höheren Pflanzen. Bd. 1: Vegetationsorgane. Berlin: Verlag von Gebrüder Borntraeger.

Turing A. (1952). The chemical basis of morphogenesis. Phil Trans Roy B. 237: 37–72.

Usugami H. (1964). Relationship between the flowering habit and the system of leaf emergence in tomato plants. Agr Hort. 39: 1281–1283.

von Veh R. (1931). Untersuchungen und Betrachtungen zum Blattstellungsproblem. Flora. 125:83-154.

Weigel D, Jürgens G. (2002). Stem cells that make stems. Nature 415: 751-754.

Weisse A. (1932). Zur Kenntnis der Blattstellungsverhaltnisse bei den Zingiberaceen. Ber Deutsch Bot Ges. 50: 327-366.

Wilkins MB, Cane AR. (1970). Auxin transport in roots: V. Effects of temperature on the movement of IAA in *Zea* roots. J Exp Bot. 21: 195-211.

Yamada H, Tanaka R, Nakagaki T. (2004). Sequences of symmetry-breaking in phyllotactic transitions. Bull Math Biol. 2004; 66: 779–789.